

RESEARCH ARTICLE SUMMARY

CANCER

Determining the ERK-regulated phosphoproteome driving KRAS-mutant cancer

Jennifer E. Klomp, J. Nathaniel Diehl, Jeffrey A. Klomp, A. Cole Edwards, Runying Yang, Alexis J. Morales, Khalilah E. Taylor, Kristina Drizyte-Miller, Kirsten L. Bryant, Antje Schaefer, Jared L. Johnson, Emily M. Huntsman, Tomer M. Yaron, Mariaelena Pierobon, Elisa Baldelli, Alex W. Prevatte, Natalie K. Barker, Laura E. Herring, Emanuel F. Petricoin III, Lee M. Graves, Lewis C. Cantley, Adrienne D. Cox, Channing J. Der*, Clint A. Stalnecker*

INTRODUCTION: Mutationally activated KRAS causes persistent activation of the RAF-MEK-ERK mitogen-activated protein kinase (MAPK) cascade. Whereas RAF and MEK kinases phosphorylate a highly restricted set of substrates, the closely related ERK1 and ERK2 serine/threonine kinases directly or indirectly phosphorylate a diversity of functionally distinct proteins. Analyses of the “logical suspects” have validated the roles of specific ERK substrates (e.g., MYC and FRA1), yet a systemwide determination of ERK substrates that facilitate mutant KRAS-driven oncogenesis remains to be completed.

RATIONALE: Nearly four decades after the discovery of KRAS mutations in cancer, clinically effective inhibitors of KRAS have been approved for KRAS^{G12C}-mutant non-small-cell

lung cancer. However, only <50% of patients respond initially, and most responsive patients become resistant and relapse within 6 months. DNA sequencing of tumors and circulating tumor DNA (ctDNA) from relapsed patients identified mutational activation (e.g., of RAF or MEK) or inactivation (e.g., NFI) of components within the RAS signaling network that result in reactivation of ERK MAPK signaling. Although numerous mass spectrometry analyses have collectively identified >1300 ERK1/2 direct or indirect substrates, the limited overlap among different studies suggests that the full spectrum of ERK-dependent phosphorylation events has not been elucidated. In this study, we applied mass spectrometry using improved methodology and pooled data from a panel of heterogeneous cancer cell lines to generate a system-wide deter-

mination of the ERK-dependent phosphoprotein signaling network in the most KRAS-addicted cancer, pancreatic ductal adenocarcinoma (PDAC).

RESULTS: Previous phosphoproteomic studies to catalog ERK substrates used a diversity of cell types, involved different ERK activation stimuli, and applied varied experimental designs. We focused on pathologic ERK signaling driven by endogenous oncogenic KRAS in PDAC. We first developed constitutively activated variants of ERK1 and ERK2 and showed that they play redundant roles. Each alone is sufficient to support mutant KRAS-dependent PDAC growth, and they stimulate nearly identical transcriptional signaling outputs. Next, evaluating phosphorylation changes caused by pharmacologic inhibition of ERK, we captured immediate direct activities (1 hour) and delayed secondary activities (24 hours) induced by loss of chronic ERK activation. We identified 2123 ERK-dependent phosphoproteins, 67% of which were not previously associated with ERK, thus greatly expanding the depth and breadth of the ERK-regulated phosphoproteome. We then applied our recently annotated serine/threonine kinase motif database to establish the protein kinase signaling network that drives the ERK-dependent phosphoproteome. At 1 hour, loss of ERK- and RSK (a direct ERK substrate)-dependent phosphorylation predominated. By contrast, at 24 hours, loss of cyclin-dependent kinase (CDK1-6)-dependent phosphorylation predominated, accompanied by activation of other kinases, indicating dynamic alterations over time. Integrating pathway analyses and information from the Cancer Dependency Map portal (DepMap), we showed that 17% of the ERK phosphoproteome is essential for PDAC growth, and it is enriched in nuclear-localized proteins and in proteins involved in cell cycle regulation and RHO guanosine triphosphatase (GTPase) signaling. The PDAC-derived KRAS-dependent phosphoproteome is driven nearly exclusively through ERK and is applicable to other tissues and species.

CONCLUSION: This study greatly expanded the depth and breadth of ERK-regulated direct and indirect phosphoproteins. Given that reactivation of ERK is a major basis for acquired resistance to KRAS inhibitor therapy, this comprehensive molecular portrait of mutant KRAS-driven pathologic ERK signaling will be important to elucidate the mechanisms of patient response and resistance to KRAS inhibitors. ■

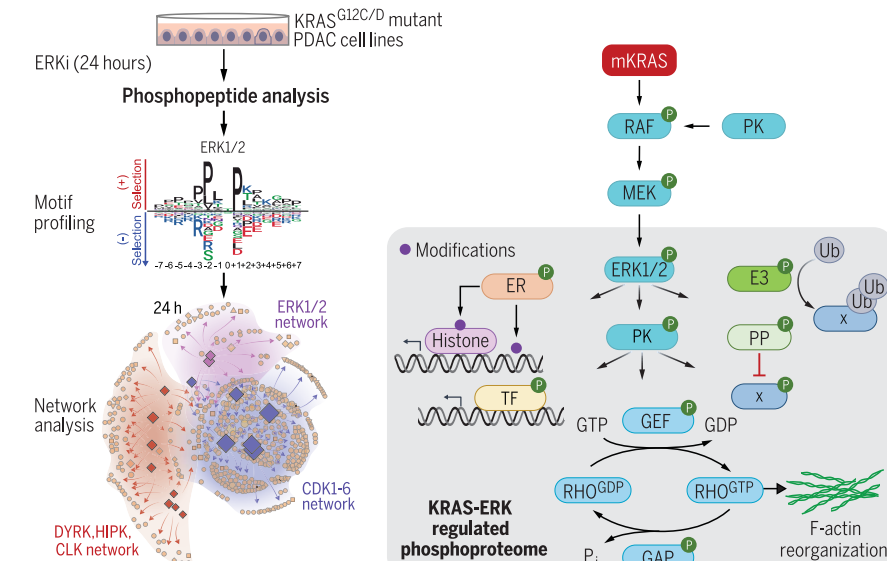
The list of author affiliations is available in the full article online.

*Corresponding author. Email: cjder@med.unc.edu (C.J.D.); clints@email.unc.edu (C.A.S.)

Cite this article as J. E. Klomp et al., Science 384, eadk0850 (2024). DOI: 10.1126/science.adk0850

S READ THE FULL ARTICLE AT

<https://doi.org/10.1126/science.adk0850>



ERK regulates a complex phosphoproteome. Phosphoproteomic analyses established the ERK-regulated phosphoproteome. Kinome motif analyses established the kinase network that drives ERK-regulated phosphorylation. ERK substrates include protein kinases (PK) and phosphatases (PP) that extend the ERK-regulated phosphoproteome and transcription factors (TF) and epigenetic regulators (ER) that drive the ERK-dependent transcriptome. Major outputs of ERK signaling regulate the cell cycle (CDKs) and RHO GTPases. ERKi, ERK1/2-selective inhibitor SCH772984; HIPK, homeodomain-interacting protein kinase; CLK, CDK-like protein kinase; DYRK, dual-specificity tyrosine phosphorylation-regulated kinase; GDP, guanosine diphosphate; GTP, guanosine triphosphate; mKRAS, mutant KRAS; GEF, guanine nucleotide exchange factor; GAP, GTPase activating protein; Pi, inorganic phosphate; Ub, ubiquitin.

RESEARCH ARTICLE

CANCER

Determining the ERK-regulated phosphoproteome driving KRAS-mutant cancer

Jennifer E. Klomp¹, J. Nathaniel Diehl², Jeffrey A. Klomp^{1,3}, A. Cole Edwards⁴, Runying Yang¹, Alexis J. Morales¹, Khalilah E. Taylor¹, Kristina Drizytle-Miller¹, Kirsten L. Bryant^{1,3}, Antje Schaefer^{1,3}, Jared L. Johnson^{5,6,7}, Emily M. Huntsman^{7,8}, Tomer M. Yaron^{7,8,9}, Mariaelena Pierobon¹⁰, Elisa Baldelli¹⁰, Alex W. Prevatte¹¹, Natalie K. Barker¹¹, Laura E. Herring¹¹, Emanuel F. Petricoin III¹⁰, Lee M. Graves^{1,3,11}, Lewis C. Cantley^{5,6,7}, Adrienne D. Cox^{1,3,4,12}, Channing J. Der^{1,2,3,4*}, Clint A. Stalnecker^{1,3*}

To delineate the mechanisms by which the ERK1 and ERK2 mitogen-activated protein kinases support mutant KRAS-driven cancer growth, we determined the ERK-dependent phosphoproteome in KRAS-mutant pancreatic cancer. We determined that ERK1 and ERK2 share near-identical signaling and transforming outputs and that the KRAS-regulated phosphoproteome is driven nearly completely by ERK. We identified 4666 ERK-dependent phosphosites on 2123 proteins, of which 79 and 66%, respectively, were not previously associated with ERK, substantially expanding the depth and breadth of ERK-dependent phosphorylation events and revealing a considerably more complex function for ERK in cancer. We established that ERK controls a highly dynamic and complex phosphoproteome that converges on cyclin-dependent kinase regulation and RAS homolog guanosine triphosphatase function (RHO GTPase). Our findings establish the most comprehensive molecular portrait and mechanisms by which ERK drives KRAS-dependent pancreatic cancer growth.

Mutational activation of the *KRAS* oncogene is a major genetic driver of pancreatic ductal adenocarcinoma (PDAC) growth (1). The best-studied immediate KRAS effectors are the RAF serine-threonine kinases (ARAF, BRAF, and RAF1 or CRAF) (2–4). Active RAS-GTP binds to and promotes activation of RAF kinase activity. Activated RAF then phosphorylates and activates the highly related dual-specificity mitogen-activated protein kinase (MAPK) kinases MEK1 and MEK2 (MEK1/2), which in turn phosphorylate and activate the highly related ERK1 and ERK2 (ERK1/2) serine-threonine kinases (5, 6).

Whereas RAF and MEK exhibit highly restricted substrate utilization, ERK substrate utilization is broad and diverse (5, 6). How ERK drives KRAS-mutant cancer growth remains poorly understood. In our recent determination of the KRAS- and ERK-dependent transcriptome in KRAS-mutant cancers (7), we found that the transcriptional output of KRAS is largely driven by ERK. We also determined that reactivation of ERK by MEK alone was sufficient to drive near-complete resistance to KRAS^{G12C} and KRAS^{G12D} mutant-selective inhibitors. These findings, as well as the significant divergence of our KRAS mutant-dependent transcriptome from the Molecular Signatures Database hallmark KRAS signature (8), provided the rationale for our current study to determine the ERK-dependent phosphoproteome. We focused on pathologic ERK signaling driven by endogenous oncogenic *KRAS* in the most KRAS-addicted cancer, PDAC, that has a 95% *KRAS* mutation frequency.

Results

ERK1 and ERK2 support KRAS-dependent growth

We recently determined that activated MEK1 but not AKT1 is sufficient to render PDAC cells insensitive to direct pharmacologic inhibition of mutant KRAS (7). Unlike MEK1, activating mutations in ERK are not found in cancer, likely because single-point mutations alone are not sufficient for full activation and therefore act as relatively weak oncogenes (9). To determine the degree to which ERK activation is sufficient to support KRAS-driven PDAC

growth, we generated constitutively activated variants of ERK1 and ERK2 (83% identity) by combining previously described point mutations that each alone increase ERK1 and ERK2 activity (9–11) (Fig. 1A). Transient doxycycline (Dox)-inducible expression of each ERK1 mutant in the KRAS^{G12D}-mutant PDAC cell line Pa16C (fig. S1A) demonstrated that the double mutant ERK1^{R84S/S170D} (designated ERK1^{SD}) most strongly induced phosphorylation of the ERK substrate FRA1 (pFRA1) (fig. S1B). We selected this and the analogous mutant of ERK2 (ERK2^{R67S/S153D}, ERK2^{SD}) for further analyses (Fig. 1A).

We established Dox-inducible expression of MYC epitope-tagged ERK1^{SD} or ERK2^{SD} in KRAS^{G12C} (MIA PaCa-2 and UM53)- or KRAS^{G12D} (Pa16C)-mutant PDAC cell lines (fig. S1A). Dox treatment stimulated ERK1/2^{SD} expression at levels comparable to that of endogenous ERK without substantially altering phosphorylation of the ERK substrate ribosomal protein S6 kinase (pRSK) or expression of MYC, which is stabilized by direct ERK phosphorylation (12) (Fig. 1B and fig. S1C). We then evaluated whether expression of ERK1^{SD} or ERK2^{SD} mutants would impact the ability of pharmacologic inhibitors targeting different nodes of the KRAS-ERK MAPK cascade to inhibit PDAC growth.

As expected, ERK1/2^{SD}-expressing cells were resistant to the MEK1/2-selective inhibitor trametinib (MEKi) (fig. S1D) but retained sensitivity to the ERK1/2-selective inhibitor SCH772984 (ERKi) (Fig. 1C). Thus, activated ERK1/2^{SD}-expressing cells retained ERK-dependent growth upon MEK inhibition. As anticipated, treatment with either a KRAS^{G12C}-selective inhibitor (MRTX1257, analog of adagrasib or MRTX849; G12Ci) (13) or the clinical candidate KRAS^{G12D}-selective inhibitor (MRTX1133; G12Di) (14) reduced MYC and pRSK levels in control cells, which was rescued by ERK1/2^{SD} expression (Fig. 1B and fig. S1C). Unexpectedly, given the role of multiple other effectors in supporting KRAS driver function in PDAC (15), we observed that activated ERK alone was able to cause complete to near-complete resistance to growth inhibition (Fig. 1C). However, this result is consistent with genetically engineered mouse models in which pancreatic expression of mutationally activated *Braf*^{V600E} but not *Pik3ca*^{H1047R} phenocopied mutant *Kras*^{G12D} to drive development of metastatic PDAC (16). This result is also consistent with the ~200-fold-greater affinity of RAS-GTP for RAF versus phosphatidylinositol 3-kinase α (PI3K α) (17, 18) and with a system-wide proteomic assessment of RAS association with 56 effectors showing that RAS-RAF is the predominant RAS-effector complex (19).

An unresolved issue is whether the highly related ERK1 and ERK2 isoforms (83% identity)

¹Lineberger Comprehensive Cancer Center, University of North Carolina at Chapel Hill, Chapel Hill, NC 27599, USA.

²Curriculum in Genetics and Molecular Biology, University of North Carolina at Chapel Hill, Chapel Hill, NC 27599, USA.

³Department of Pharmacology, University of North Carolina at Chapel Hill, Chapel Hill, NC 27599, USA. ⁴Cell Biology and Physiology Curriculum, University of North Carolina at Chapel Hill, Chapel Hill, NC 27599, USA. ⁵Department of Cell Biology, Harvard Medical School, Boston, MA 02115, USA.

⁶Dana-Farber Cancer Institute, Harvard Medical School, Boston, MA 02115, USA. ⁷Meyer Cancer Center, Weill Cornell Medicine, New York, NY 10065, USA. ⁸Englander Institute for Precision Medicine, Institute for Computational Biomedicine, Weill Cornell Medicine, New York, NY 10021, USA. ⁹Columbia University Vagelos College of Physicians and Surgeons, New York, NY 10032, USA. ¹⁰School of Systems Biology, George Mason University, Fairfax, VA 22030, USA.

¹¹UNC Michael Hooker Proteomics Center, University of North Carolina at Chapel Hill, Chapel Hill, NC 27599, USA. ¹²Department of Radiation Oncology, University of North Carolina at Chapel Hill, Chapel Hill, NC 27599, USA.

*Corresponding author. Email: cjder@med.unc.edu (C.J.D.); clints@email.unc.edu (C.A.S.)

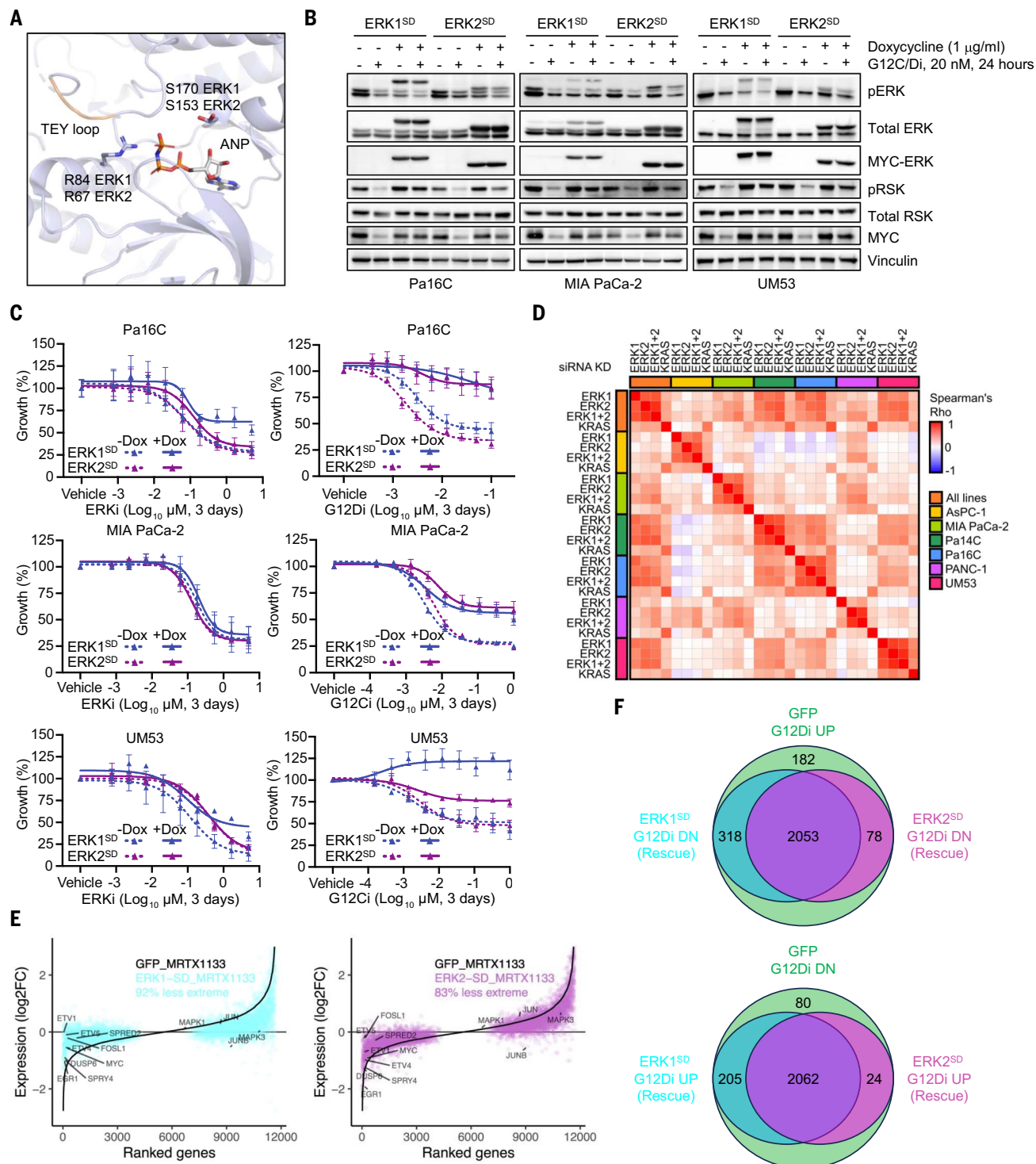


Fig. 1. ERK signaling is critical for KRAS-regulated PDAC growth. (A) Crystal structure of ERK2 bound to the ATP analog phosphoaminophosphonic acid-adenylate ester (ANP); activating ERK2 mutations (and analogous ERK1 mutations) and the TEY activation loop are shown (PDB: 4NIF). (B) Immunoblots showing mutant ERK expression and rescue of downstream signaling in Pa16C, MIA PaCa-2, and UM53 cells with Dox-inducible activated ERK1^{SD} (R84S/S170D) or ERK2^{SD} (R67S/S153D) treated with the KRAS^{G12D} (MRTX1133, 20 nM) or KRAS^{G12C} (MRTX1257, 20 nM) inhibitor for 24 hours. Dox (1 μ g/mL) was added 24 hours prior to drug treatments. Blots are representative of three or more independent experiments. Quantification of pRSK and MYC are shown in fig. S1C.

(C) Cell viability assays of Pa16C, MIA PaCa-2, and UM53 cells with Dox-inducible expression of activated ERK1^{SD} (R84S/S170D) or ERK2^{SD} (R67S/S153D) in response to KRAS^{G12C/D} (MRTX1257, MRTX1133) or ERK1/2 inhibitor (SCH772984). Dox treatment (1 μ g/mL) was added 24 hours prior to drug treatments. Graphs show the mean percent growth of three replicates \pm standard error of the mean. (D) RPPA Spearman correlation coefficients comparing $\log_2(FC)$ of signals from 147 antibodies for the individual six cell lines and all cell lines considered together. Cells were treated with siRNAs targeting NS (nonspecific control), KRAS, MAPK3 (ERK1), and/or MAPK1 (ERK2) for 72 hours as in fig. S1E. Statistical analysis was performed from four biological replicates. The individual treatments and full protein list can be

found in fig. S1G and data S1. (E) RNA transcript expression changes induced by 24-hour KRAS^{G12D} inhibition (MRTX1133, 100 nM) versus DMSO control in Pa16C cells expressing activated ERK1^{SD} (cyan), ERK2^{SD} (pink), or GFP control (black). Genes are ranked by expression changes in GFP-expressing cells. Dox (1 μg/mL) was added 24 hours prior to drug treatments. Statistical analysis was performed from two biological replicates. Genes shown for ERK1^{SD} and ERK2^{SD} (points) are those with significant differential expression induced by KRAS^{G12D} inhibition in GFP control cells (adjusted $P < 0.01$). (F) Venn diagrams representing the overlap between genes up-regulated (G12Di UP) or down-regulated (G12Di DN) by KRAS^{G12D} inhibition in GFP-expressing cells (green: $|log_2FC| > 0.25$,

adjusted $P < 0.01$) and genes rescued by ERK1^{SD} (cyan) and ERK2^{SD} (pink). The center overlap (purple) depicts genes rescued by both ERK1^{SD} and ERK2^{SD}, the genes in only the green area are not rescued by either, those in the cyan area are rescued by only ERK1^{SD}, and those in the purple area are rescued by only ERK2^{SD}. The term “rescue” indicates an expression change (log_2FC) less extreme than the GFP control but no p-values were used to represent the degree of those expression changes. Single-letter abbreviations for the amino acid residues referenced throughout this paper are as follows: G, Gly; C, Cys; T, Thr; E, Glu; Y, Tyr; D, Asp; F, Phe; S, Ser; P, Pro; N, Asn; A, Ala; L, Leu; V, Val; I, Ile; K, Lys; H, His; R, Arg.

possess distinct or redundant biological functions (20). Our finding that either activated ERK1 or ERK2 alone can drive resistance to KRAS inhibition (Fig. 1C) supports their overlapping functions in promoting KRAS-dependent PDAC growth. To further address this question, we performed acute small interfering RNA (siRNA)-mediated suppression of either *MAPK3* (ERK1) or *MAPK1* (ERK2) alone or concurrently and evaluated the consequences for signaling and growth in four KRAS^{G12D}-mutant and two KRAS^{G12C}-mutant PDAC cell lines (fig. S1, E and F). We also included *KRAS* suppression to assess the role of ERK in KRAS function.

We determined that siRNA suppression of either *MAPK3* (ERK1) or *MAPK1* (ERK2) alone strongly impaired PDAC growth, comparable to suppression of *KRAS* itself. Although this result would be consistent with distinct functions of ERK1 and ERK2, it is also consistent with the prevailing evidence for a threshold requirement for the total combined level of ERK1 and ERK2 rather than for isoform-selective functions (20).

To determine whether ERK1 and ERK2 regulate distinct signaling activities, we performed reverse-phase protein array (RPPA) profiling of 147 established signaling proteins and phosphorylation events in six KRAS^{G12C/D}-mutant PDAC cell lines (fig. S1, A and G, and data S1). Spearman correlations of the signaling changes observed upon ERK1 or ERK2 suppression were high, indicating that the signaling changes were nearly identical, supporting the conclusion that their functions are redundant rather than distinct (Fig. 1D, and fig. S1, H and I). Providing further support for redundant functions of ERK1 and ERK2, we found that ectopic expression of ERK1^{SD} or ERK2^{SD} attenuated nearly all G12Di-induced transcriptional changes (by 92 and 83%, respectively) (Fig. 1, E and F). The signaling changes caused by acute siRNA suppression of *KRAS* and *ERK* were similar, differing primarily in their relative intensities (fig. S1I). Together, these observations support redundant signaling outputs of ERK1 and ERK2 in supporting KRAS-dependent growth.

ERK-dependent phosphoproteome in KRAS-mutant PDAC

Recently, Ünal *et al.* created a compendium of ERK substrates (21) by collating the data from

an earlier compilation of ERK substrates (22) together with 12 mass spectrometry-based phosphoproteomic analyses and the PhosphoSitePlus (PSP) database. The resulting compendium was composed of 2507 ERK-dependent phosphosites on 1310 proteins, of which 26% were defined as direct ERK phosphosites. This ERK compendium of direct and indirect ERK substrates (21) did not include any data derived from KRAS-mutant pancreatic cancer (fig. S2A). Therefore, we determined the ERK-dependent phosphoproteome in KRAS-mutant PDAC cell lines. Further, whereas most previous studies evaluated ERK substrates under conditions of transient ERK activation such as EGF stimulation, our analysis focused on ERK substrates under conditions of pathologic ERK activation driven by mutant KRAS.

We used the adenosine triphosphate (ATP)-competitive and allosteric ERKi SCH772984, shown by *in vitro* studies with purified recombinant protein kinases to be highly selective for ERK1/2. To assess its selectivity in PDAC cell cultures, we used the well-established multiplexed kinase inhibitor beads and mass spectrometry (MIB-MS) assay (23). MIB-MS and related proteomics assays have reliably provided kinome-wide determination of on- and off-target cellular activities of protein-kinase inhibitors (24). Previous studies delineating ERK substrates have typically used a single cell line (fig. S2A). Despite the near 100% occurrence of *KRAS* mutations in PDAC, PDAC is genetically heterogeneous, with most other mutations occurring at single-digit frequencies (1). Therefore, we evaluated a panel of six KRAS^{G12C/D}-mutant PDAC cell lines treated acutely (1 hour) or long term (24 hours) with SCH772984 (Fig. 2A). Using MIB-MS, we found selective inhibition of only ERK1 and ERK2 out of 207 protein kinases quantified at both time points (Fig. 2B and data S2). Thus, we confirmed the cellular selectivity of SCH772984 for ERK1 and ERK2.

To identify the ERK-dependent phosphoproteome in KRAS-mutant human cancer, we performed quantitative phosphoproteomics using phosphopeptide enrichment and liquid chromatography–tandem mass spectrometry (LC-MS/MS) in the same panel of six *KRAS*-mutant PDAC cell lines (Fig. 2C). To optimize detection of direct ERK substrates, we treated

cells acutely for 1 hour. To capture both primary and secondary consequences of ERK inhibition, we performed long-term 24-hour treatment with ERKi, a time point when compensatory activities begin to appear owing to loss of ERK negative feedback regulation (6). Altogether, we detected a total of 13,646 distinct total phosphosites across all six cell lines. Of these, 932 were differentially regulated at 1 hour of ERKi, and 4288 were differentially regulated by 24 hours (Fig. 2D and data S3). At 1 hour, phosphosites were predominantly down-regulated, whereas by 24 hours, a considerable fraction was up-regulated.

A comparison of our PDAC ERK-dependent phosphoproteome with the ERK substrate compendium showed overlap of only 12% (580) phosphosites and 33% (707) phosphoproteins (Fig. 2E). To account for phosphosites attributed to other kinases not included in the compendium, we expanded our analysis to include the Post-Translational Modification Signatures Database (PTMsigDB) and the known regulatory sites reported by the PSP database (25), which together showed 29% (735/2507) overlap with the ERK Compendium. Our PDAC ERK phosphoproteome showed a 21 and 60% overlap at the phosphosite and phosphoprotein levels, respectively, with the combined substrates from these three datasets.

Similar to our analyses, the ERK compendium data were derived from analyses of cancer-derived cell lines maintained in artificial cell culture conditions (fig. S2A). We therefore compared our ERK-dependent phosphoproteome with a recent proteomics study of pancreatic cancer patients that profiled the proteome and phosphoproteome in bulk tumor tissue, including adjacent nontumor regions, collected by the NCI Clinical Proteomic Tumor Analysis Consortium (CPTAC) (26). Our ERK-dependent phosphoproteome had a higher degree of overlap with this *in vivo* PDAC-specific dataset at both the phosphosite and protein levels: 32 and 77%, respectively (Fig. 2E). The incomplete overlap likely reflects the low cellularity of PDAC, which is typically composed of only 10 to 15% tumor tissue (1). Furthermore, their analyses included only treatment-naïve PDAC, few of which were metastatic (26), whereas we evaluated cell lines derived from both primary and metastatic PDAC tumors.

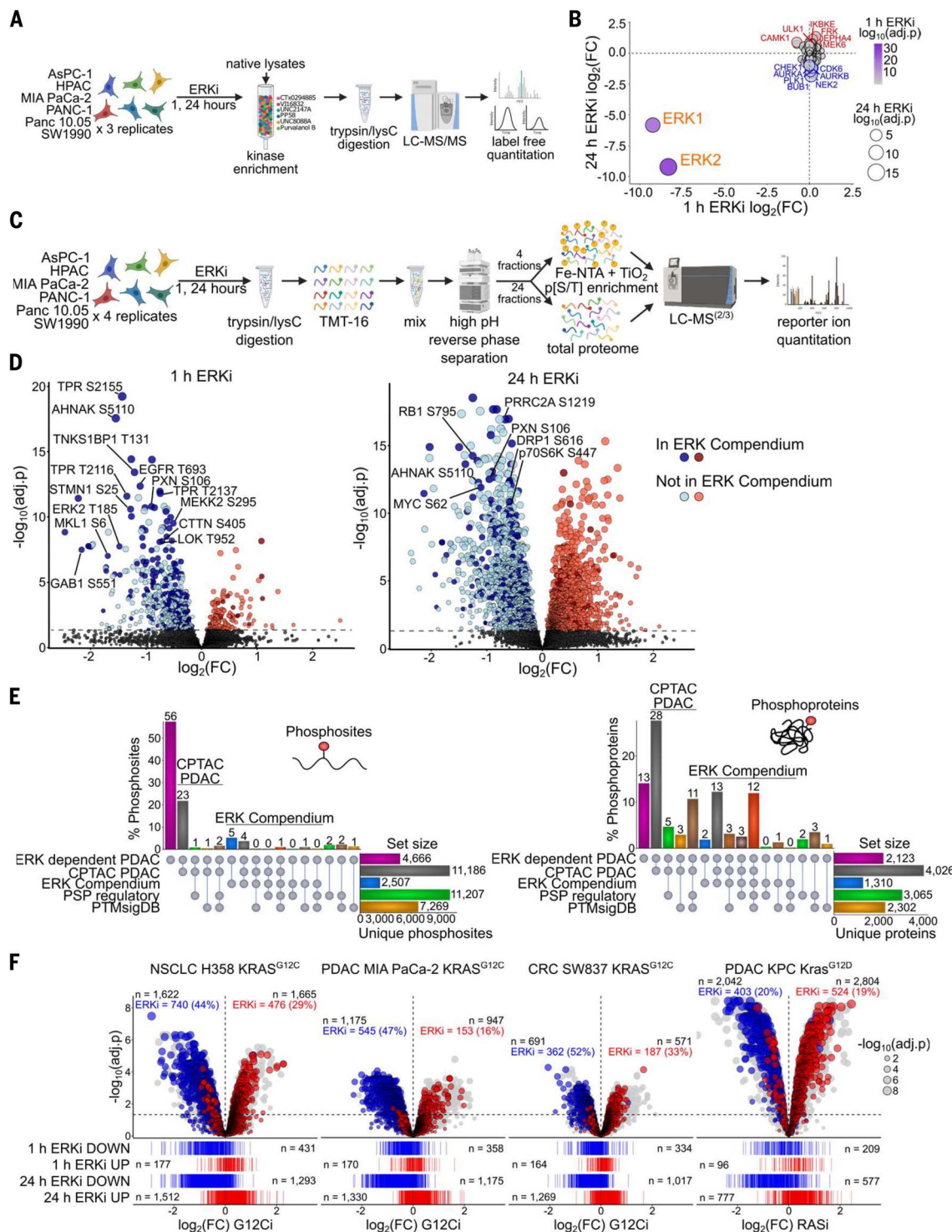


Fig. 2. Phosphoproteomic determination of the ERK-regulated phosphoproteome in KRAS-mutant PDAC. (A) Flow diagram of the MIB-MS experiment was created with BioRender.com. (B) MIB-MS analyses of six KRAS-mutant cell lines treated for 1 or 24 hours with ERKi (SCH772984, 1 μ M). (C) Experimental workflow for proteomics analyses, created with BioRender.com. (D) Differentially expressed phosphosites following 1 and 24 hours ERK inhibition in the same six PDAC cell lines as in (A) and (B). Phosphosites previously reported in the ERK Compendium are highlighted, and the top significantly dysregulated sites identified within the ERK compendium as direct substrates of ERK are labeled.

(E) Overlap between ERK-dependent phosphosites ($P < 0.05$) or phosphoproteins in PDAC and phosphosites or phosphoproteins reported in the CPTAC PDAC dataset (FDR < 0.05), ERK compendium, PSP regulatory sites, and PTMsigDB. (F) Differentially expressed phosphosites following 24-hour KRAS^{G12C} inhibition (MRTX1257, 20 nM, G12Ci) or RAS(ON) multiselective tricomplex inhibition (RMC-7977, 10 nM, RASI). ERK-dependent phosphosites ($P < 0.05$, 24 hours) are annotated by blue (down-regulated) or red (up-regulated) points. ERK-regulated phosphosites at 1 and 24 hours are annotated as bars below the volcano plot.

This suggests that our dataset is more representative of human PDAC and highlights its inclusion of >2500 (>50%) phosphosites and >200 (>10%) proteins not found in any of the existing databases.

To establish how many of these phosphosites have potential regulatory functions, we compared our ERK-dependent phosphoproteome with a recent study that compiled 6801 proteomics experiments from human cells and used machine learning techniques to assign functional significance (27). We found 91% overlap with the functional phosphoproteome phosphosites with a median functional score of 0.43 (fig. S2, B and C). This is within a similar range to that of the ERK compendium (0.47) and known regulatory sites reported in PSP (0.51) and PTMsigDB (0.54) (fig. S2C). Furthermore, when including all sites reported in PSP, only 157 sites in our ERK-dependent phosphoproteome (3%) cannot be found in any of these datasets (fig. S2B).

Two key factors contributed to the extensive depth of our dataset, such that >50% of our ERK-regulated phosphoproteome has not been reported in previous datasets: (i) We applied improved proteomics methodology enabling increased phosphosite coverage (table S1) (28–30). (ii) Whereas previous ERK phosphoproteomic analyses typically used a single cell line, our analyses of six PDAC cell lines allowed us to compensate for cell line heterogeneity.

We noted considerable heterogeneity in phosphosite coverage between cell lines, identifying from 4000 to 10,000 total distinct phosphosites and variable numbers of ERK-regulated sites at 1 hour and 24 hours (fig. S2D). We determined that the heterogeneity of ERK-regulated sites was not related to ERK inhibitor sensitivity, but rather due to the limitation of LC-MS/MS proteomics methods to detect peptides in independent experiments. Although phosphosite detection was variable across cell lines, 75% of ERK-dependent phosphosites were detected in at least two cell lines, and we found high correlations of phosphosite changes between cell lines at each time point (fig. S2, E and F). We performed differential expression analysis of phosphosites by considering every possible combination of one, two, three, four, and five versus all six cell lines (fig. S2G). We found that the number of distinct phosphosites identified as ERK regulated was highly dependent on how many cell lines were considered. Notably, we found that these numbers converged on our analysis of all six cell lines that modeled cell line-specific changes. The combined dataset of six cell lines provided the highest correlation of phosphosite changes observed for any one cell line (fig. S2H). We validated a subset of 64 phosphosite and protein changes using our previously published comprehensive RPPA dataset of 13 KRAS-mutant PDAC cell lines treated for 24 hours

with an equivalent concentration of SCH772984 (31). We found good agreement for those ERK-regulated phosphosites and proteins that have readily available antibodies (fig. S2, I and J). Taken together, the improved methodology applied to identify the phosphoproteome and our use of multiple cell lines contributed to the substantial extension of direct and indirect ERK substrates identified in our PDAC ERK-regulated phosphoproteome.

To determine the generality of our ERK-regulated phosphoproteome and validate our findings, we evaluated its overlap with the KRAS-dependent phosphoproteome in lung, colorectal, and pancreatic cancer cell lines. We additionally included a *Kras*-mutant mouse PDAC (KPC; *Kras*^{G12D}; *Trp53*^{R172H}) tumor-derived cell line to establish cross-species validation. We determined the phosphoproteome in KRAS^{G12C} mutant H358 non-small-cell lung cancer (NSCLC), SW837 colorectal cancer (CRC), and MIA PaCa-2 PDAC cell lines treated with a pharmacological inhibitor of KRAS^{G12C} (MRTX1257) or in the KPC mouse PDAC tumor-derived cell line treated with a RAS(ON) multiselective tricomplex inhibitor RMC-7977 (RASI) (data S4 and S5) (32). We found that our ERK-dependent phosphoproteome was enriched in the KRAS^{G12C}-dependent phosphoproteomes in human cell lines, particularly among down-regulated phosphosites, where it accounted for >44% of differentially regulated phosphosites (Fig. 2F). To compare our ERK-dependent phosphoproteome in the KPC mouse cell line, we mapped the human phosphosites to the mouse reference proteome using homology alignment. Sequence alignment revealed 577 ERK-down-regulated and 777 ERK-up-regulated overlapping phosphosites. Among the overlapping phosphosites, 403 (70%) and 524 (67%) were significantly down- or up-regulated upon treatment with RASI, respectively. When considering all overlapping phosphosites between each dataset, we found high correlations (fig. S2K). These observations validate our ERK-dependent phosphoproteome as a core component of the KRAS-regulated phosphoproteome and extend our findings to the widely studied KPC mouse model.

ERK regulates a global phosphoproteome enriched in ERK interaction motifs

Extracellular stimuli promote transient ERK phosphorylation and activation, resulting in ERK translocation from the cytoplasm to the nucleus (5, 6). To assess the subcellular distribution of activated ERK under conditions of sustained activation by mutant KRAS, we applied two approaches. First, we performed immunofluorescence using an ERK1/2 phosphospecific antibody that recognizes MEK1/2 phosphorylation at the ERK1/2 TEY motif. We detected steady-state phosphorylated ERK (pERK) and total ERK throughout the cell, including localization within the nucleus (Fig. 3,

A and B, and fig S3, A and B). Following 24 hours of ERKi treatment, pERK levels were strongly suppressed both outside and inside the nucleus. Concurrently, consistent with loss of ERK signaling, we observed decreased expression of the ERK substrate MYC (fig. S3, C and D). Secondly, because pERK may not accurately monitor ERK activity, we used a set of ERK kinase activity reporters (EKAR4) targeted to cytoplasmic (cyto-EKAR4) or nuclear (nuc-EKAR4) compartments (29). These reporters likewise showed strong suppression of both cytoplasmic and nuclear ERK activity following 24 hours of ERKi treatment (Fig. 3, C and D, and fig. S3, E and F).

We next evaluated the ERK-dependent phosphoproteome for the subcellular distribution of ERK-regulated phosphoproteins. We observed changes in phosphoproteins associated with every major organelle (Fig. 3E), consistent with ERK regulating a global phosphoproteome spanning all subcellular compartments (27). Down-regulated phosphoproteins were enriched in cytoskeletal proteins at both 1 and 24 hours of ERK inhibition. At 24 hours, down-regulated phosphoproteins were also enriched in nuclear proteins, whereas up-regulated phosphoproteins were enriched in plasma membrane-associated proteins.

We then determined gene set enrichment for the subcellular compartments enriched in ERK-regulated phosphoproteins. At 1 hour, down-regulated cytoskeleton-associated phosphoproteins were involved in mitosis and RAS homolog (RHO) small guanosine triphosphatase (GTPase) signaling (fig. S3G). At 24 hours, additional cell cycle- and mitosis-related gene sets were associated with the cytoskeleton, with RHO GTPase signaling still enriched but no longer among the top 10 significant gene sets (fig. S3H and data S6). Nuclear-associated phosphoproteins exhibiting down-regulated phosphosites revealed more cell cycle-related pathways, including S phase, G2/M checkpoints, DNA replication, RNA polymerase II transcription, tRNA processing, and mRNA transport (fig. S3I). Phosphoproteins associated with the plasma membrane exhibiting up-regulated phosphosites were enriched in receptor tyrosine kinase (RTK) signaling, transport of small molecules, apoptotic proteins, and cell-cell communication (fig. S3J). Taken together, we found that ERK inhibition led to changes in phosphorylation throughout the cell, with enrichment in subcellular localizations that differed between 1 and 24 hours of ERK inhibition. The top pathways among ERK-regulated subcellular compartments are involved in the regulation of cell cycle transitions, replication, RHO GTPase signaling, and RTK activation.

ERK regulates diverse signaling pathways through direct substrate interactions that propagate to secondary, indirect interactions that

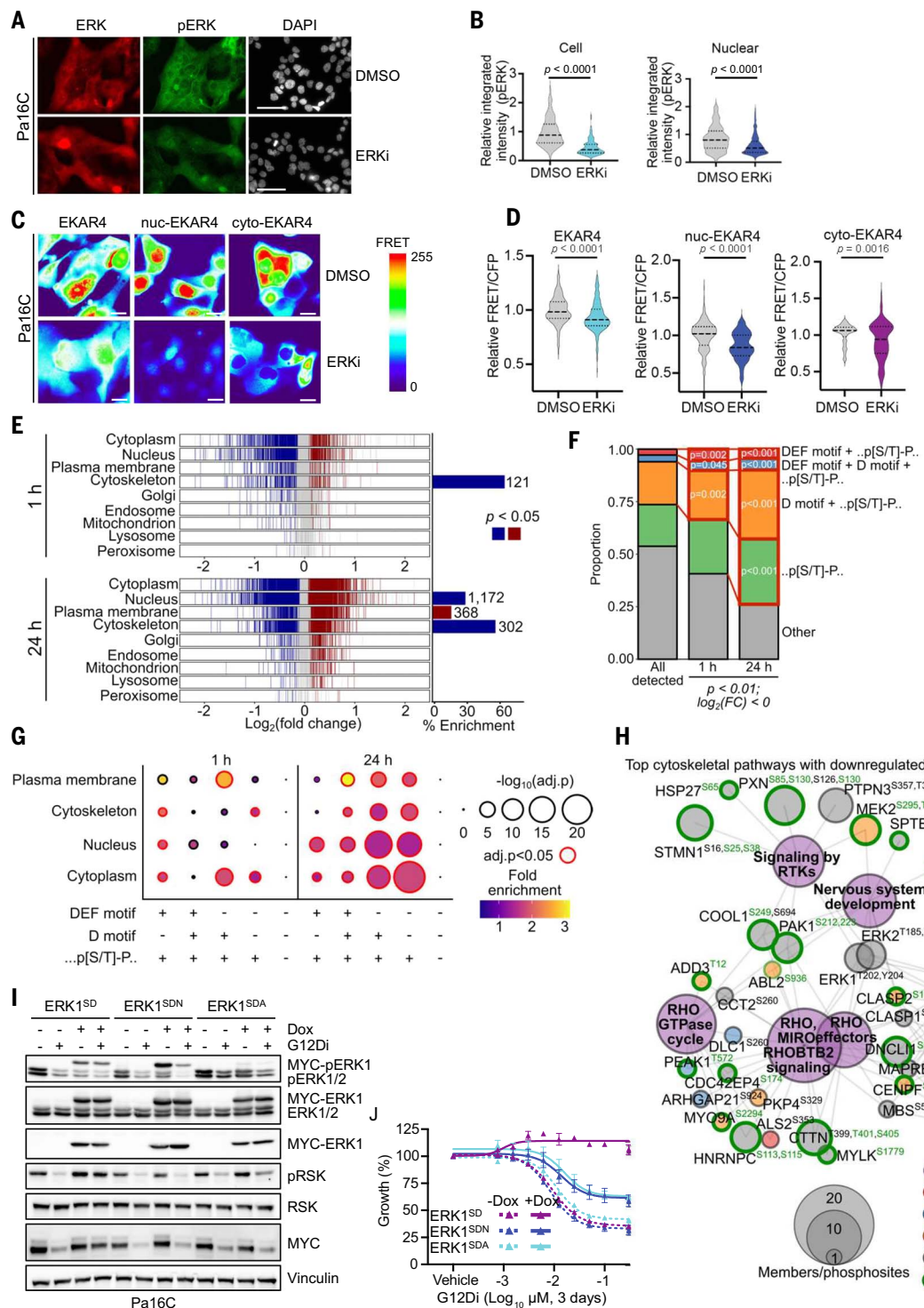


Fig. 3. The ERK phosphoproteome regulates diverse functional pathways comprised of proteins enriched in ERK binding motifs. (A) Representative images of pERK (red), total ERK (green), and nuclear DAPI (gray) immunofluorescence in Pa16C cells treated with ERKi (SCH772984, 1 μ M) or DMSO for 24 hours (scale bar, 75 μ m), quantified in (B). (B) Dashed lines represent the median, and statistics represent a Mann-Whitney test on 113 to 655 individual cells from 5 to 10 fields of at least two replicates. (C) Representative pseudocolored FRET intensity of Pa16C cells stably expressing untagged EKAR4 (EKAR4) or EKAR4 tagged with either a nuclear localization signal (nuc-EKAR4) or nuclear export signal (cyto-EKAR4) treated with ERKi (SCH772984,

1 μ M) or DMSO for 4 or 24 hours (scale bar, 20 μ m), quantified in (D). (D) Statistical analysis performed as in (B). (E) Subcellular association of phosphoproteins with differentially regulated phosphosites and enrichment (red or blue, $P < 0.05$) at 1 and 24 hours ERKi treatment. Statistical analysis of enrichment determined by one-tailed hypergeometric testing and P values corrected by Benjamini-Hochberg. (F) Proportion of phosphosites containing the p[S/T]-P phospho-motif together with an ERK-binding D or DEF motif within the phosphoprotein. Proportions were determined within the background of all detected phosphosites and sites differentially down-regulated at 1 and 24 hours ERKi treatment [$P < 0.01$, $\log_2(FC) < 0$]. Statistical analysis of enrichment

determined as in (E). (G) Subcellular association of phosphoproteins with ERK binding and phosphorylation motifs as in (F). Point color and size represent relative enrichment and significance of enrichment, respectively. Points are highlighted if statistically enriched (red, adjusted $P < 0.05$). Enrichment was determined by using one-tailed hypergeometric enrichment with all detected phosphosites as background. (H) Membership of phosphoproteins within top enriched gene sets for cytoskeleton-associated phosphoproteins with down-regulated phosphosites at 1 hour ERKi treatment. Phosphoproteins are colored by the presence of ERK-binding D or DEF motifs and outlined in green if a differentially regulated phosphosite was detected with a p[S/T]-P motif. Phosphoprotein size is proportional to the number of down-regulated phosphosites, and pathways are sized by the number of phosphoprotein members.

Differentially regulated phosphosites are also shown and likewise colored green if the phosphosite contains a p[S/T]-P motif. (I) Immunoblots showing mutant ERK expression and downstream signaling in Pa16C-expressing Dox-inducible ERK1^{SD}, ERK1^{SDN} (R84S/S170D/D338N), and ERK1^{SDA} (R84S/S170D/Y280A) treated with the KRAS^{G12D} inhibitor (MRTX1133, 20 nM) for 24 hours. Dox (1 μ g/mL) was added 24 hours prior to drug treatments. Blots are representative of three or more independent experiments and quantification of pRSK and MYC are in fig. S3Q. (J) Viability of Dox-inducible ERK1^{SD}, ERK1^{SDN}, and ERK1^{SDA} cell lines treated with a dose escalation of G12Di (MRTX1133). Dox (1 μ g/mL) was added 24 hours prior to drug treatments. Graphs show the mean percent growth of three replicates \pm standard error of the mean.

promote ERK activity at the subcellular level (5, 6). One approach that can provide an approximate indication of direct ERK substrates is to characterize the phosphoproteins for the presence of the minimal ERK phosphorylation motif, [S/T]-P (33), together with two distinct ERK docking sequences, DEF (also called docking site for ERK FXF or F) and D (also called DEJL) motifs (34). These ERK docking sites enhance the specificity and affinity of ERK substrate association. We found enrichment in all three ERK-directed motifs at each time point among the down-regulated phosphosites, with ~75% having the [S/T]-P motif and ~40% having a D and/or DEF motif together with [S/T]-P (Fig. 3F). Subcellular localization of ERK can direct ERK-regulated processes (35), and ERK-interacting motifs have been suggested to direct ERK activity to substrates in distinct subcellular compartments (36). Therefore, we determined the subcellular enrichment of ERK-interacting motifs among ERK-regulated phosphoproteins and found distinct patterns, with D motifs enriched in each compartment and DEF motifs primarily localized to nuclear proteins (Fig. 3G and fig. S3K). We then evaluated the identified ERK-regulated subcellular pathways for ERK-binding and phosphorylation motifs. We found a high frequency of proteins containing DEF, D, and [S/T]-P motifs. At 1 hour of ERKi treatment, ERK-binding motifs were found in 43% (16/37) of the cytoskeleton-associated phosphoproteins in the top enriched pathways, and 62% (23/37) contained a [S/T]-P ERK phosphorylation motif (Fig. 3H). This increased to 57% (24/42) and 81% (34/42) of phosphoproteins with ERK-binding and [S/T]-P ERK phosphorylation motifs, respectively, among cytoskeleton-associated phosphoproteins at 24 hours of ERKi treatment (fig. S3L). Among nuclear-associated phosphoproteins enriched at 24 hours of ERKi treatment, 55% (113/204) contained ERK-binding motifs, and 72% (286/398) a [S/T]-P motif (fig. S3M). These results highlight that ERK can engage a multitude of phosphoprotein candidates throughout subcellular compartments to impact diverse cellular processes.

We next evaluated the importance of ERK interaction with D- and DEF motif-containing

proteins in supporting KRAS-dependent PDAC growth. Point mutations that selectively impair rat ERK2 interaction with D- or DEF motif-containing substrates but not its kinase function have been described previously (36). We introduced the analogous amino acid substitutions into activated human ERK1^{SD} or ERK2^{SD} to generate variants impaired in interaction with D motif-containing [D338N (ERK1^{SDN}) and D321N (ERK2^{SDN})] or DEF motif-containing [Y280A (ERK1^{SDA}) and Y263A (ERK2^{SDA})] substrates. Pa16C cells stably infected with lentivirus vectors encoding each ERK1/2 mutant were then treated with Dox to transiently express each ERK mutant prior to treatment with various inhibitors (Fig. 3I and fig. S3N). As shown previously, ERK1/2^{SD}-expressing cells were resistant to G12Di or MEKi treatment while remaining sensitive to ERKi, whereas this resistance was lost in the ERK1/2^{SDN/SDA} mutants (Fig. 3J and fig. S3, O, P, and Q). Ectopic expression of ERK1/2^{SDN} or ERK1/2^{SDA} was unable to rescue ERK activation (pRSK and MYC) in cells treated with G12Di (Fig. 3I and fig. S3N). Thus, ERK interaction with D and DEF motifs is required to mediate ERK signaling critical for KRAS dependent growth.

ERK regulates a complex network of protein kinases

ERK substrates include proteins regulating gene transcription, protein phosphorylation, and protein homeostasis that drive ERK-dependent secondary signaling to alter the global transcriptome, proteome, and phosphoproteome. Therefore, we next evaluated our ERK-dependent phosphoproteome for phosphosite changes on these broad classes of proteins (Fig. 4A). Following 1 hour of ERK inhibition, we found decreased phosphosites on 33 epigenetic regulators, 31 transcription factors, 28 kinases, 16 E3 ligases, and 5 phosphatases. At 24 hours, these numbers increased to 107, 98, 55, 44, and 13, respectively. More than half contained the ERK-interacting DEF and/or D motifs. Many of these proteins have known regulatory phosphosites, enabling us to evaluate changes in phosphorylations with reported regulatory consequences. After

1 hour of ERK inhibition, we found decreased regulatory phosphorylations on 3 epigenetic regulators, 10 transcription factors, 12 kinases, and 1 E3 ligase. Known associations with cancer pathogenesis include CBX3 S93, MYC S62, FRA1 S265, FOXO3 S294, epidermal growth factor receptor (EGFR) T693, RAF1 S29/S642, p70S6KB S423, and NIPA S344. Similarly, at 24 hours of ERK inhibition, we found decreased regulatory phosphorylations on 16 epigenetic regulators, 19 transcription factors, 19 kinases, and 8 E3 ligases. These phosphoproteomic results are consistent with our comparison of the ERK-dependent transcriptome and proteome in KRAS-mutant PDAC, where we identified transcriptional signatures attributable to ERK-regulated transcription factors (7). Furthermore, we found that some ERK-dependent proteins were regulated at the protein level but not transcriptionally, suggesting E3 ligase-dependent protein turnover (7). Together, these results support ERK-dependent regulation of a complex transcriptome, proteome, and phosphoproteome.

To gain a better understanding of the dynamics of kinase regulation following ERK inhibition, we made use of the most comprehensive catalog of kinase-motif specificities to date. Recently, we utilized a synthetic peptide library to profile the substrate sequence specificity of essentially all functional human serine-threonine kinases in vitro (37). We applied this unbiased dataset to determine how ERK inhibition alters the frequency of down- or up-regulation of each kinase motif. We assigned a relative kinase activity score to each kinase, using the frequency factor and significance to represent how frequently the kinase motif was differentially regulated (Fig. 4B and fig. S4, A and B). Overall, we found dysregulation of cyclin-dependent kinases (CDKs), MAPKs, glycogen synthase kinases (GSKs), and CDK-like kinases (CLKs) (collectively, the CMGC group of kinases) involved in growth and cell cycle regulation (fig. S4, C and D). After 1 hour of ERK inhibition, the most down-regulated kinase motifs were those of ERK1 and ERK2 (Fig. 4B and fig. S4A), consistent with the high selectivity of this ERKi. Among other down-regulated kinases were ERK-effector

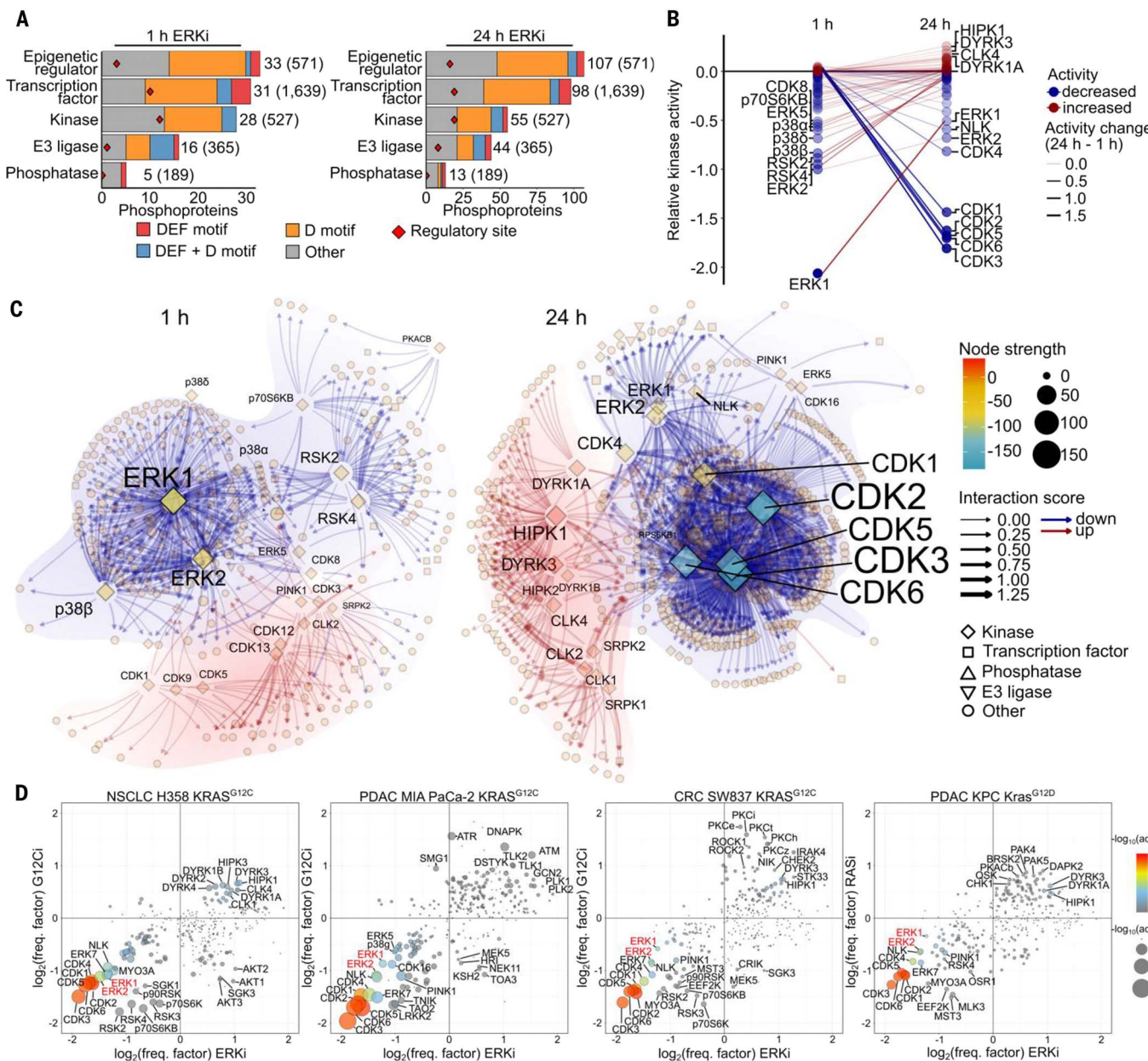


Fig. 4. ERK regulates a dynamic phosphoproteome by engaging downstream kinases. **(A)** Epigenetic regulator, transcription factor, kinase, phosphatase, and E3 ubiquitin ligase phosphoproteins with down-regulated phosphosites and their ERK-binding DEF and/or D motifs. The number of phosphoproteins containing a down-regulated known regulatory phosphorylation is annotated with a red triangle. **(B)** Relative kinase activities calculated for 303 S/T kinases at 1 and 24 hours of ERKi treatment by using kinase-motif specificities (37). Line color represents the direction of change from 1 to 24 hours ERKi treatment, and line transparency represents the magnitude of change. **(C)** Kinase-substrate networks at 1 and 24 hours of ERKi treatment. Networks were constructed using kinase-motif specificities (37), kinase-substrate specificities from

PhosphoSitePlus (25), kinase-substrate interactions from PhosphoNetworks (38), and BioGRID (39). Nodes are sized and colored by their strength in network, and shape represents protein group. Edges are colored by direction of association with up- or down-regulated phosphosites. Edge width represents the magnitude of interaction score. The top quantile of kinases is labeled in each network, and text size is scaled with node strength. **(D)** Comparison of kinase-motif enrichment [$\log_2(\text{frequency factor})$] derived from ERK-dependent versus RAS-dependent phosphoproteomes as shown in Fig. 2F. Fill color represents the significance of enrichment in the ERK-dependent phosphoproteome, and size represents the significance in the KRAS^{G12C}- or RAS-dependent phosphoproteome.

kinases, the RSKs (RSK2, RSK4, and p70S6KB), along with other MAPKs (ERK5 and p38α/β/γ), whereas, after 24 hours of ERK inhibition, we observed strong down-regulation of CDKs (CDK1 to CDK6; CDK1-6) (Fig. 4B and fig. S4B). Although ERK1/2 activity remained sig-

nificantly depressed at 24 hours, it had rebounded compared to activity at 1 hour (Fig. 4B). Notably, ERK1 rebound was greater than ERK2, perhaps reflecting differential regulation of their kinase activity despite their identical phosphorylation motif preferences (fig. S4E).

Similarly, kinases downstream of ERK, such as the RSKs, had rebounded by 24 hours. We also observed up-regulation of the related homeodomain-interacting protein kinases (HIPKs), CLKs, and dual-specificity tyrosine phosphorylation-regulated kinases (DYRKs)

that have not been identified previously as ERK targets. These global motif analyses revealed unexpected insights into the complexity and dynamics of kinase reprogramming that occurs after ERK inhibition.

Kinase-substrate relationships remain challenging to predict as they are highly transient and rely on many factors such as colocalization, affinity, and kinase regulation. We used our recently established in vitro kinase motif specificities and kinase activities dataset (37) together with the kinase-phosphosite specificities cataloged by the PSP kinase substrate database, the kinase-substrate binding interactions in PhosphoNetworks (38), and interactors cataloged by BioGRID (39). Accounting for the activities of phosphatases in our analysis was also challenging because their motif specificities and substrates are less well defined. Nevertheless, we performed enrichment analyses of potential phosphatase-substrate relationships from BioGRID and found dysregulation of only a few phosphatases, namely the ERK-selective dual-specificity phosphatases (DUSP2, DUSP3, and DUSP6), cell cycle control phosphatases (CDC14B and CDC25A), and AGC kinase phosphatases (PHLPP1/2) (fig. S4, F and G). Therefore, we focused on kinase-substrate specificities and changes we observed in our phosphoproteomics data to develop a network analysis method (fig. S4H).

This network assigns interaction scores for every phosphosite in our dataset using supporting data from kinase-phosphosite and kinase-phosphoprotein interactions (fig. S4I). Notably, this method incorporates previously reported kinase-substrate relationships, which is heavily biased toward the most-studied kinases, by strengthening kinase-substrate interactions we derived by motif analysis (data S7). Kinase-substrate interactions that have not been previously reported but are supported by motif specificities remain a main component of the network, and this is reflected in their interaction score. For example, top-scoring interactions were mainly attributed to *MAPK3* (ERK1), driven mostly by motif specificity score and further increased by interactions reported in previous datasets (fig. S4I). Despite their identical phosphorylation motif preferences, ERK1 displayed slightly higher activity than ERK2 in our in vitro kinase assay (fig. S4E), which biased interactions more toward ERK1 than ERK2 in our analyses.

Using this kinase-substrate network, we evaluated the top-scoring interactions and differential kinase activities following 1 and 24 hours of ERK inhibition (Fig. 4C and fig. S4J). Following 1 hour of ERK inhibition, the down-regulated kinase networks were mainly attributed to ERK1/2, RSK2/4, and p70S6KB. Motif analysis of phosphosites attributed to ERK from this network revealed an enrichment of the prototypical [P/L/V/I]-X-p[S/T]P

motif (fig. S4K). Additionally, when we considered positional depletion, we noted strong negative selection of basic residues (K and R) at the -3 position and acidic residues (D and E) at positions +1 to +3. This further defines the stringency of ERK1/2 phosphomotifs. We then analyzed RSK2/4 phosphosites and found enrichment of basic residues at positions N-terminal to the phosphorylation site, consistent with previous studies (40), and depletion of proline at +1 (fig. S4K), exhibiting mutually exclusive substrate preferences as ERK and targeting a distinct subset of phosphorylation sites. These motifs have been well characterized (25, 37), validating our network construction.

The cyclin-dependent kinases CDK1-6 make up the predominant down-regulated phosphorylation network after prolonged ERK inhibition (Fig. 4C). Whereas CDK substrates overlapped with a subset of ERK substrates, ERK1/2 also maintained a distinct group of substrates. CDKs are also CMGC family proline-directed kinases, and therefore, distinguishing CDK from ERK MAPK phosphosites relies on subtle motif differences. When we investigated CDK1-6 phosphorylations from our network, we found the motif to be enriched for proline at +1, as expected, and basic residues (K and R) at the +3 position (fig. S4K). This is consistent with the motif specificity that we reported, where there was a near complete requirement of K and R at +3 for CDK activity (37). We also observed a depletion of basic residues N-terminal to the phosphorylation site and acidic residues in the C-terminal region, further adding specificity to these kinase motifs. With ERK1/2 and CDK1-6 having similar but distinct motif specificities, these results highlight the high probability that ERK and CDK target sequences overlap (e.g., [P/L/V/I]-X-[S/T]-P-X-[K/R]). When we evaluated our ERK regulated sites for this sequence, we found 266 phosphosites, half of which contained D or DEF motifs (132/266). Furthermore, these sites are found on mediators of PDAC growth, for example, MYC at S62 (P-L-S*-P-S-R), that are likely to be under convergent regulation by MAPKs and CDKs.

Unexpectedly, after sustained ERK inhibition, we observed up-regulation of a group of kinases not known to be ERK substrates, including HIPK (HIPK1 to HIPK3; HIPK1-3), DYRK (DYRK3 and DYRK1A and DYRK1B; DYRK1A/B), and CLK (CLK1 to CLK4; CLK1/4) kinases (Fig. 4, B and C, and fig. S4, B and D). We speculate that these comprise compensatory mechanisms to offset the deleterious cellular consequences of ERK inhibition. Consistent with this possibility, our DepMap analyses found that several (HIPK1, DYRK1A/B, and CLK1/4) showed genetic dependencies in PDAC comparable to that of ERK1 (*MAPK3*) and ERK2 (*MAPK1*) (fig. S4L). These proline-directed

kinases make up a distinct branch of CMGC kinases (fig. S4D). The phosphorylation motif enrichment pattern for DYRK family kinases favored proline residues in the +1 and +3 positions with basic residues N-terminal to the phosphorylation site (fig. S4K). This p[S/T]-P-X-P motif has been previously attributed to ERK1/2 (21). However, our motif and network analyses revealed that, although the DYRK, HIPK, and CLK kinases are proline directed, they are likely targeting a distinct subset of S/T-P substrates from those of ERK1/2 or CDK1-6 and are regulated in the opposite direction in response to ERK inhibition. These results further suggest that they represent a group of substrates resulting from compensatory activities due to prolonged ERK inhibition.

We then investigated the mechanisms of the robust down-regulation of CDK activity by sustained ERK1/2 inhibition. CDKs are regulated at the level of transcription, posttranslational modification, and through protein-protein interactions with their cyclin activators (41). We found that all CDKs were down-regulated by 24 hours, both transcriptionally and at the protein level, along with many of their associated regulatory cyclins (fig. S4M). However, we noted that cyclins B1 and B2 were the most significantly down-regulated proteins even though their transcript levels were unchanged, suggesting that their protein levels are regulated through degradation. We found decreased phosphosites on members of the anaphase-promoting complex/cyclosome (APC/C) proteins known to regulate cyclins B1 and B2. After 1 hour of ERK inhibition, we observed down-regulation of ANAPC1 S688 and ANAPC3 (CDC27) S344, which was attributed to ERK1/2 (fig. S4N). By 24 hours of ERK inhibition, we found several down-regulated phosphosites on CDC20 (S41, T59, T106, and T170) and FZR1 (T121), both of which are known regulatory components of the APC/C (fig. S4M). Taken together, we found that ERK inhibition leads to a coordinated collapse of CDK activity regulated at the levels of gene transcription, protein phosphorylation, and protein degradation. This collapse of essentially every key cell cycle-regulatory CDK contributes to the potent cell cycle arrest, rather than apoptosis, caused by ERK inhibition in KRAS-mutant PDAC cells (42, 43).

We then evaluated the dysregulated kinases in our KRAS-regulated phosphoproteomes. Although KRAS can engage multiple effectors to regulate a diverse network of signaling cascades, we found few differences between ERK- and KRAS-regulated kinases (Fig. 4D). Notably, the PI3K effector AKT was down-regulated in only one of four cell lines (H358). The most consistently down-regulated kinases across the KRAS-regulated kinomes were the cyclin-dependent CDKs, ERK MAPKs, and RSKs. Up-regulated kinases showed more cell line

heterogeneity, with HIPK and DYRK kinases the most consistent, validating our findings from the ERK-dependent kinase. Few KRAS-regulated kinases were significantly dysregulated in the opposite direction to ERK. This is consistent with our observation that ERK activity is sufficient to rescue KRAS inhibition and is enriched in the KRAS-regulated phosphoproteome.

ERK is highly integrated with RHO signaling

To gain mechanistic insight into the cellular processes regulated by the PDAC ERK phosphoproteome compared with the ERK compendium, we performed pathway analysis using all gene sets in the Gene Ontology (GO), Kyoto Encyclopedia of Genes and Genomes (KEGG), and Reactome databases. We compared the overlap of both significantly enriched gene sets and all terms, significant or not, associated with each ERK-regulated phosphoprotein list (Fig. 5A and fig. S5A). Despite only 33% phosphoprotein identity (Fig. 2E), we found 66% overlap of the PDAC ERK-dependent phosphoproteome with the ERK compendium (Fig. 5A and fig. S5A). Although the nonoverlapping enriched gene sets exceeded the number of overlapping sets (674 nonoverlapping versus 563 overlapping) by using the above criteria, the overlap was greater (85%) when we considered any associated GO, KEGG, or Reactome terms.

Our dataset was most enriched in genes encoding proteins related to RHO GTPase signaling pathways (Fig. 5B), which were also among the top gene sets enriched in the ERK Compendium. The top pathways significantly enriched in our PDAC ERK-dependent phosphoproteome that were not significant in the ERK compendium were related to chromatin organization, RNA processing, and G1/S cell cycle components (Fig. 5B). Thus, our identified ERK-dependent phosphoproteome revealed a more comprehensive profile of the role of aberrant ERK activation in supporting KRAS-dependent cellular properties of PDAC.

We also found that the shorter 1-hour ERK inhibition altered kinases and substrates distinct from those altered upon longer 24-hour ERK inhibition. Therefore, we evaluated gene set enrichment using Reactome gene sets in down- and up-regulated phosphoproteins at both time points. After 1 hour of ERK inhibition, we found enrichment of RHO GTPase- and EGFR- or MAPK-associated signaling pathways in the down-regulated phosphoproteins (Fig. 5C and data S8). No gene sets were enriched among the up-regulated phosphosites. By 24 hours of ERK inhibition, we found a different set of significantly enriched pathways among down- and up-regulated phosphoproteins. Down-regulated phosphoproteins were enriched in components of the cell cycle, mitosis, chromosome maintenance, DNA damage, and replication. Notably, contrary to the enrichment of RHO GTPase phosphoproteins

with down-regulated phosphorylations after 1 hour of ERK inhibition, at 24 hours, these same RHO-regulated pathways were enriched among the up-regulated phosphoproteins. The distinct nature of processes altered upon longer-term ERK inhibition likely reflects secondary activities initiated by the acute loss of ERK function, particularly compensatory activities in response to the growth suppression induced by ERK inhibition.

We then focused on RHO GTPase-associated genes to examine their switch from enrichment in down-regulated phosphoproteins after 1 hour of ERK inhibition to enrichment in up-regulated phosphoproteins after 24 hours of ERK inhibition. We analyzed the phosphosites on proteins within the RHO GTPase Reactome pathway and how these changed over time (fig. S5B). Very few phosphosites down-regulated at 1 hour were up-regulated after 24 hours. Instead, up- and down-regulated phosphosites were distinct at each time point. We then used our phosphorylation network consisting of both time points to isolate the proteins and respective kinases within these gene sets (Fig. 5D). This analysis revealed three distinct regulatory networks: The first consists of ERK substrates with down-regulated phosphosites after 1 hour of ERK inhibition. The second consists of CDK1/2/3/5/6 substrates down-regulated after 24 hours of ERK inhibition, which shared a subset of substrates with ERK1/2. The third is composed of up-regulated phosphosites on a distinct group of protein substrates driven by putative compensatory activation of kinases PKN1/2, PAK4/6, PDPK1, and DYRK, HIPK, CLK, and SRPK.

The RHO GTPase-associated kinases PKN1/2, PAK4/6, and PDPK1 have well-described associations with regulation of RHO-dependent F-actin cytoskeletal reorganization, indicating that our network analysis identified mechanistically relevant associations. The network interactions responsible for identifying PKN1/2, PAK4/6, and PDPK1 were composed of distinct phosphorylation motifs (fig. S5C) that were found on actin cytoskeleton-associated proteins, such as EXOC2, PXN, AHNAK, or SHROOM3 (fig. S5D).

RHO GTPase signaling is dynamic and complex; consequently, RHO signaling pathway genes overlap with numerous other cellular functions. To further characterize ERK-dependent changes in the RHO GTPase network, we identified proteins that had either down- or up-regulated phosphorylations upon ERKi treatment at either timepoint then performed gene enrichment analyses. Among the proteins with down-regulated phosphorylations, we found that RHO GTPase signaling overlapped considerably with gene sets encoding proteins related to RTK signaling and cell cycle regulation (fig. S5E). However, up-regulated phosphorylations were associated primarily with

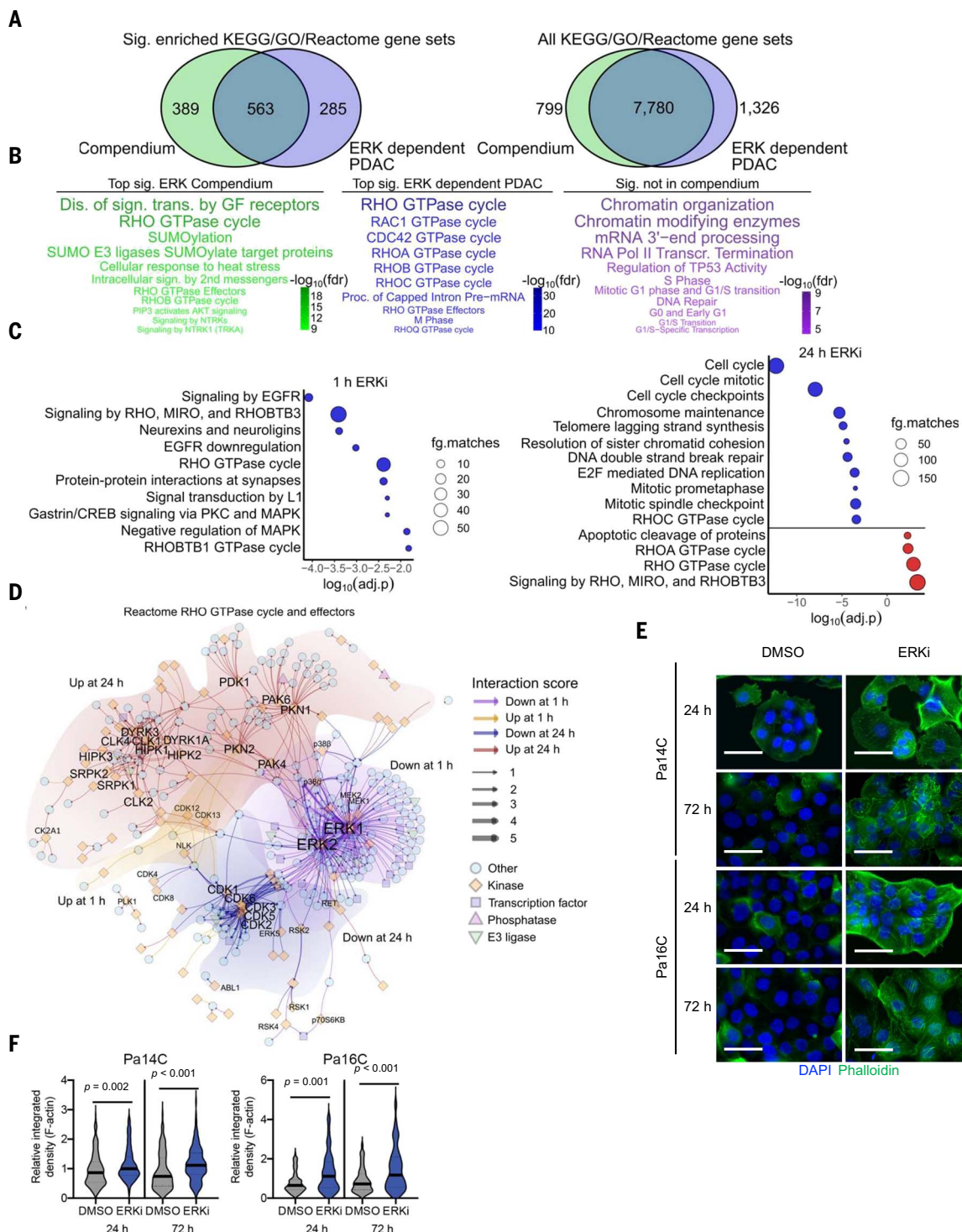
more restricted RHO GTPase gene sets, such as RAC1, RAC3, CDC42, and RHOA. The only RHO GTPase-associated proteins that contained both down- and up-regulated phosphorylations were PXN, MYPT1 (*PPP1R2A*), EMS1 (*CTTN*), PI14RhoGEF (*ARHGEF18*), PARG1 (*ARHGAP29*), and SCRIB1 (*SCRIB*). We considered that these phosphorylation changes could be secondary to changes in total protein levels. However, few proteins were altered in their expression levels, and no consistent trends were observed (fig. S5F). The up-regulated phosphorylations were largely associated with regulation of RHO GTPase activity. By contrast, the down-regulated phosphorylations are largely associated with functional pathways such as cellular growth control and morphology that are in turn regulated by the confluence of signaling from RTKs, MAPKs, and RHO GTPases.

A well-studied consequence of RHO activation is promotion of actin cytoskeleton reorganization that drives alterations in cellular morphology (44). We used immunofluorescence microscopy to evaluate changes in actin stress fibers following 24 and 72 hours of ERK inhibition. Consistent with our phosphoproteomics analyses, an increase in actin stress fibers was observed within 24 hours of ERK inhibition and continued at and beyond 72 hours (Fig. 5, E and F). These results were also consistent with our observations of cellular flattening and increased cell size (fig. S5, G and H) during growth assays following ERK inhibition. RHO promotion of actin stress fibers can activate YAP1 (44), a well-validated driver of KRAS independence (45, 46). Consistent with RHO activation acting as a compensatory mechanism, RHOA and YAP1-TEAD activation was identified as a basis for acquired resistance to adagrasib in KRAS^{G12C}-mutant cancer cell lines (47, 48).

ERK regulates proteins critical for PDAC growth

Although specific ERK substrates have been evaluated for their involvement in driving the growth of KRAS-mutant PDAC (e.g., MYC) (49), a system-wide determination of the full spectrum of ERK-regulated proteins that drive cancer cell growth remained to be done. To begin to elucidate the cancer driver components of the ERK-dependent phosphoproteome in PDAC, we first evaluated the genetic dependency of all ERK regulated phosphoproteins using the genome-wide CRISPR-Cas9 data on 43 KRAS-mutant PDAC cell lines in the DepMap database. Of the 1636 genetic dependencies (median Chronos < -0.5) identified in KRAS-mutant PDAC cell lines, we detected 690 in our phosphoproteomics dataset, more than half (362) of which had ERK regulated phosphosites (fig. S6A).

We and others have established that ERK-regulated proteins can be found throughout

**Fig. 5. ERK signaling is highly integrated with RHO GTPase signaling.**

(A) Overlap of KEGG, GO, and Reactome gene sets significantly enriched in (left; $P < 0.01$) or containing any gene associated with (right) phosphoproteins reported in the ERK compendium (21) or the ERK-dependent PDAC phosphoproteome. Gene set enrichment was determined by using one-tailed hypergeometric testing with the entire proteome as background for both phosphoprotein lists; P values were corrected by Benjamini-Hochberg. (B) Terms of top Reactome gene sets significantly enriched in the ERK Compendium (left), in the ERK-dependent PDAC phosphoproteome (middle), or in the ERK-dependent PDAC phosphoproteome but not the ERK compendium (right). Terms are sized and colored by significance of enrichment. (C) Signed significance from gene enrichment analysis of up- or down-regulated phosphoproteins [$\log_2(\text{FC}) < 0$ or > 0 ; adjusted $P < 0.05$] at 1 and 24 hours of ERKi. Up- and down-regulated phosphoprotein enrichment is represented by fill color (red and blue, respectively), with the number of phosphoproteins annotated as size by foreground matches. (D) Isolated network for edges connecting to proteins within the Reactome “RHO GTPase cycle” and “RHO GTPase effectors” gene sets with interaction scores greater than one standard deviation. Edges are colored by time point (1 or 24 hours), and phosphosite change (up- or down-regulated) and edge-node associations are outlined (down at 1 hour, down at

are sized and colored by significance of enrichment. (E) Signed significance from gene enrichment analysis of up- or down-regulated phosphoproteins [$\log_2(\text{FC}) < 0$ or > 0 ; adjusted $P < 0.05$] at 1 and 24 hours of ERKi. Up- and down-regulated phosphoprotein enrichment is represented by fill color (red and blue, respectively), with the number of phosphoproteins annotated as size by foreground matches. (F) Isolated network for edges connecting to proteins within the Reactome “RHO GTPase cycle” and “RHO GTPase effectors” gene sets with interaction scores greater than one standard deviation. Edges are colored by time point (1 or 24 hours), and phosphosite change (up- or down-regulated) and edge-node associations are outlined (down at 1 hour, down at

24 hours, up at 1 hour, and up at 24 hours). Top kinases by strength are labeled and node-sized by strength. (E) Representative images of phalloidin (green) and nuclear DAPI (blue) immunofluorescence in Pa14C and Pa16C cells treated with ERKi (1 μM, SCH772984) or DMSO for 24 or 72 hours (scale bar, 50 μm).

the cell. An unresolved question is whether ERK nuclear or cytoplasmic activity is more critical for cancer cell growth (50–52). We annotated the top localization scores for each protein with strong genetic dependencies in PDAC and found enrichment in nuclear-associated phosphoproteins (76%; 288/1072) (Fig. 6A). We also found an appreciable number (36%; 136/406) of cytoplasmic proteins, consistent with ERK regulating critical proteins in both the nucleus and cytoplasm.

Having found RHO GTPase-related gene sets enriched among the ERK-regulated phosphoproteins, we next evaluated the genetic dependencies of RHO GTPase phosphoproteins. Indeed, among the high genetic dependencies we found significant enrichment in RHO GTPase effectors and the more focused RHOBTB GTPase pathway. Gene set enrichment of all high-dependency ERK-regulated phosphoproteins revealed RNA metabolism and cell cycle components as top enriched pathways, particularly cell cycle pathways relating to M phase and S phase (Fig. 6A and fig. S6B). This is consistent with ERK regulating nearly every principal component of the cell cycle machinery.

We next considered whether ERK-regulated genetic dependencies were selective for *KRAS*-mutant cancers. Because >90% of PDAC cases harbor mutant KRAS, leaving few wild-type KRAS PDAC cell lines to compare, we extended our analysis to include other *KRAS*-mutant cancers with at least 10% representation of KRAS mutation frequency in DepMap (fig. S6C). We defined *KRAS*-mutant as harboring specific known KRAS driver mutations including G12A/C/D/R/S/V, G13D, or Q61K/H/L/R. We compared the genetic dependencies in cell lines harboring mutant KRAS to those in lines harboring wild-type KRAS. Of the genes with significantly greater dependencies in *KRAS*-mutant versus *KRAS*-wild-type cancers, we found 23 genes whose protein products include ERK-regulated phosphosites (Fig. 6B). These mutant KRAS-selective genetic dependencies were even more apparent in *KRAS*-mutant PDAC versus all *KRAS*-mutant cancers (Fig. 6C). This result suggests that these proteins, though important for supporting proliferation across cancer types, may be even more crucial in PDAC, perhaps owing to its higher dependence on KRAS and sustained ERK activity.

Among the top mutant KRAS-selective ERK targets were FRA1 (*FOSL1*), MYC, and p130CAS (*BCAR1*). We and others recently established essential roles for FRA1, MYC, and p130CAS in

(F) Quantification of relative integrative intensity of F-actin from (E). The solid line represents the median and dashed lines represent the upper and lower quartiles. A Mann-Whitney test was performed on 113 to 655 individual cells from 5 to 10 fields of at least two replicates.

supporting KRAS-mutant PDAC tumorigenic growth (43, 49, 53). Other genes or proteins with selective dependencies in KRAS-mutant cancer types are involved in actin cytoskeleton organization and RHO GTPase regulation [FLII, COOL1 (*ARHGEF7*), and NRPB1], epigenetic modifiers [MEP50 (*WDR77*) and RIOK1], metabolic proteins and small molecule transporters (SCAP, SCD, IMPDH2, ENO1, TPI1, NME2, EFR3A, LSM12, ABCF1, WNK1, and TRPM7), or DNA replication and RNA metabolism (DBF4, POLR1A, NIFK, and NPM1).

Having evaluated the genetic dependencies of the entire ERK-regulated phosphoproteome, we next leveraged our kinase-substrate network to attribute kinase interactions associated with high-dependency genes (Fig. 6D). This revealed genetic dependencies that were identified as ERK1/2 substrates; substrates of the downstream ERK1/2 kinases, RSK1, RSK3, and RSK4; and CDK substrates. We found that most genetic dependencies were associated with downregulated phosphosites, not up-regulated phosphosites. The highest genetic dependencies attributed to ERK1/2 phosphorylation at 1 hour of ERKi treatment were MYC, ANAPC3 (*CDC27*), ANKLE2, and ANAPC1. Notably, ANKLE2, ANAPC1, and ANAPC3 are mitotic regulators, and ANAPC1 and ANAPC3 are core components of the APC/C that regulate the CDK1 activators cyclin B1 and B2 (fig. S4, M and N). We determined that concurrent pharmacologic inhibition of APC/C and ERK synergistically suppressed PDAC growth (7).

Among the top genetic dependencies in the ERK-regulated PDAC phosphoproteome were the CDK1 regulators PKMYT1 and WEE1 as well as CDK1 itself. These observations lead to a model whereby ERK regulates phosphoproteins that drive CDK1 activation and progression through the S and M phases of the cell cycle. This activity would likely cooperate with the second most frequent genetic driver in PDAC, mutational loss of the CDK4/6-regulating tumor suppressor *CDK2NA*, which occurs at almost as high a mutational frequency (90%) as *KRAS* and is required for PDAC progression in mouse models (1, 54).

Discussion

Our delineation of the ERK-dependent phosphoproteome specifically in the setting of persistent hyperactivation in KRAS-mutant cancers has substantially expanded both the depth and breadth of ERK-regulated phosphoproteins. Together with our complementary determination of the ERK-dependent transcriptome in KRAS-mutant cancers (7), we have established

to date the most comprehensive molecular portrait of the consequences of pathologic ERK signaling, which controls a multitude of cellular processes that disrupt normal cell cycle regulation. Despite the plethora of KRAS effectors now identified, our studies nevertheless establish the dominant role of the RAF-MEK-ERK signaling network in driving KRAS-mediated oncogenesis. Our analyses also reveal the highly dynamic response of the genome to KRAS-ERK inhibition with the delayed onset of adaptive secondary or compensatory activities that may drive both primary and treatment-associated acquired resistance mechanisms to KRAS and ERK inhibition.

Specifically, we present ERK signaling as highly integrated with RHO GTPase and CDK signaling and report pathway components that will be of interest for further study to determine their functional role in supporting KRAS-mutant PDAC and other KRAS-mutant cancers. The recent approval of direct KRAS inhibitors marks a major milestone in the treatment of KRAS-mutant cancers. However, the rapid onset of acquired resistance driven largely through ERK reactivation also emphasizes that full elucidation of how ERK supports KRAS oncogenic function will be critical for the clinical advancement of KRAS inhibitors that are effective for long-term treatment of these cancers.

Materials and methods

Cell culture

Patient-derived xenograft (PDX) human PDAC cell lines (Pa01C, Pa02C, Pa03C, Pa14C, and Pa16C) were provided by Dr. Anirban Maitra (MD Anderson Cancer Center). Murine KPC tumor-derived cell line (K8484) was provided by Dr. Ken Olive (Columbia University). PDAC cell lines (AsPC-1, HPAC, MIA PaCa-2, PANC-1, and SW1990), NSCLC cell line (H358), CRC cell line (SW837), and HEK293T were obtained from American Type Culture Collection (ATCC). PDX-derived, KPC, and CRC cell lines were maintained in Dulbecco's Modified Eagle medium (DMEM) supplemented with 10% fetal bovine serum (FBS). Conventional PDAC and NSCLC cell lines were maintained in RPMI 1640 medium supplemented with 10% FBS. The identity of PDAC lines were verified by short tandem repeat analysis. All cells were tested and negative for mycoplasma.

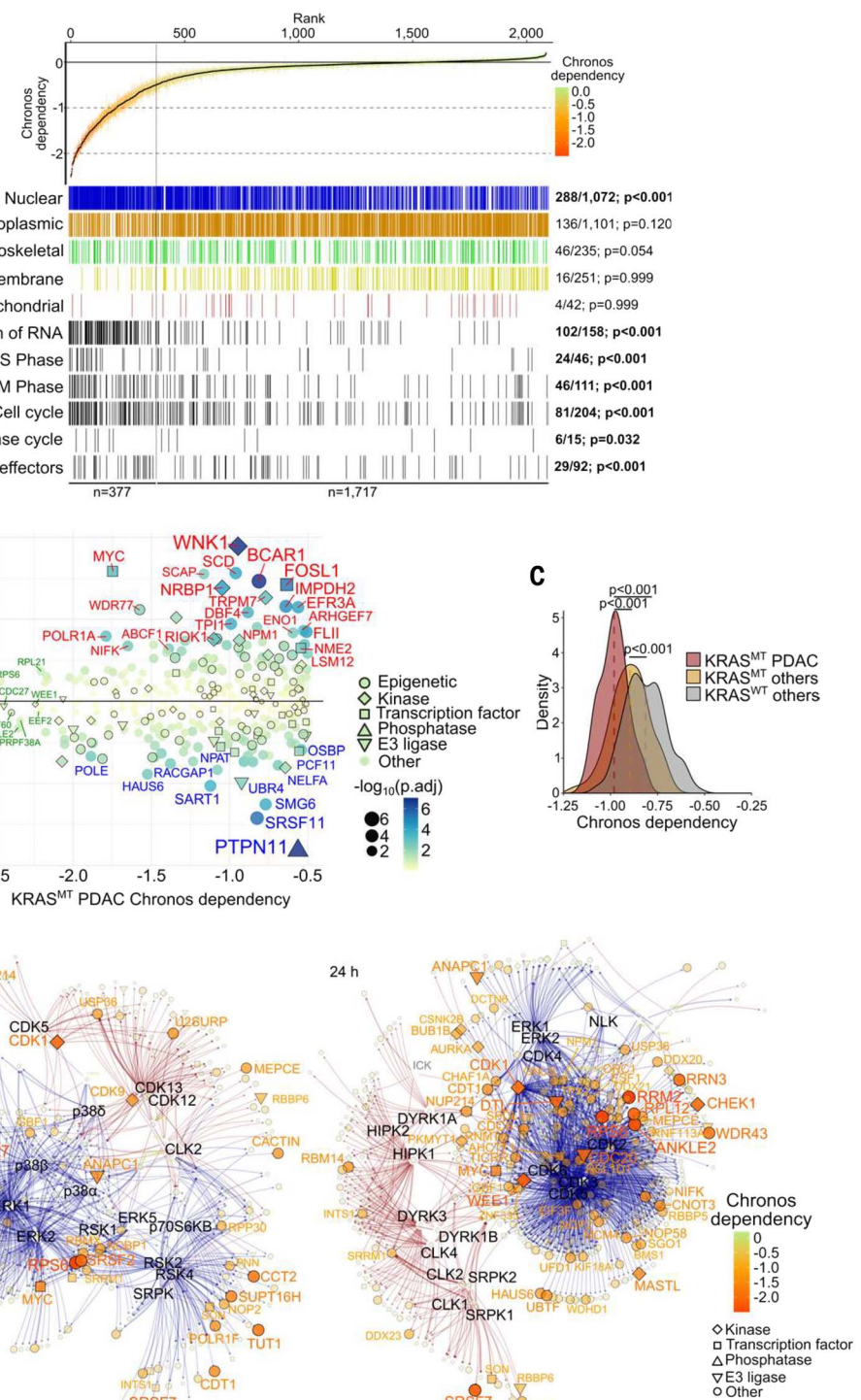
Expression plasmid constructs

ERK1 and ERK2 wild-type human cDNA was MYC-tagged and cloned into a pCEFL construct. Site-directed mutagenesis using the primers listed in table S1 were used to generate

Fig. 6. Genetic dependencies of the ERK dependent PDAC phosphoproteome. (A) Annotated Chronos dependency rank plot, ranked by DepMap dependency scores for ERK-regulated phosphoproteins. Median Chronos dependency across 43 KRAS-mutant (MT) PDAC cell lines for each phosphoprotein is represented as a point on the rank plot. The line for each point represents upper and lower quartiles and is colored by the median dependency. Annotations indicate membership in the subcellular compartment or Reactome gene set. Enrichment significance was determined by one-tailed hypergeometric testing of phosphoproteins with median Chronos scores < -0.5 (dotted line), and *P* values were corrected by Benjamini-Hochberg.

(B) Selectivity of genetic dependencies for ERK-regulated phosphoproteins toward KRAS-mutant or KRAS-wild-type (WT) cancers. Cell lines from cancers of the pancreas, large intestine, biliary tract, lung, stomach, endometrium, cervix, or ovary were characterized as either KRAS mutant, including G12A/C/D/R/S/V, G13D, or Q61K/H/L/R mutations, or KRAS wild type. The mean difference in Chronos dependency (y axis) in KRAS-mutant and KRAS-wild-type cell lines is shown for each ERK-regulated phosphoprotein with respect to the mean Chronos dependency in KRAS-mutant PDAC (x axis). Genes are colored and sized by adjusted *P* values calculated by two-way ANOVA and Tukey's HSD post hoc test between KRAS-mutant and KRAS-wild-type cell lines, with cancer type as an independent variable. (C) Density histogram of mean genetic dependencies of the 23 genes with significantly selective dependencies in KRAS-mutant cancers as shown in (B), separated by KRAS-mutant PDAC versus other cancers from (B) defined as KRAS mutant or KRAS wild type. Statistical differences were determined by Games-Howell. (D) Kinase-substrate network from 1 and 24 hours of ERKi treatment, with node size and color representing median genetic dependency of the 43 KRAS-mutant PDAC cell lines. Edges represent interaction scores as in Fig. 4C.

single, double, and triple ERK1 and ERK2 mutants. Following sequencing verification, AGE1-MYC-tagged FWD and ERK1/2-MLU1 REV primers (table S2) were used to amplify ERK1 and ERK2 cDNA containing the desired point mutation(s). The purified polymerase chain reaction (PCR) inserts and pINDUCER-EGFP



(55) were digested with AGE1 and MLU1, purified, and ligated together. Colonies were screened via sequencing upstream, downstream, and within the insertion sites to cover the entire inserted region. Resultant plasmids containing MYC-tagged ERK1 and ERK2 constructs in the pINDUCER backbone were deposited to

Addgene [Plasmid numbers: 213591 (R84S), 213592 (S170D), 213593 (R84S/S170D), 213594 (R84S/D338A), 213595 (R84S/S170D/D338N), 213596 (R84S/S170D/Y280A), 213597 (R67S/S153D), 213598 (R67S/S153D/D321N), and 213599 (R67S/S153D/Y263A)]. EKAR4 constructs with or without nuclear localization sequence

(nuc-EKAR4) or nuclear export sequence (cyto-EKAR4) were gifts from Dr. Jin Zhang (UCSD) and were described previously (35, 56). Using the EKAR-BAMH1 FWD and UT/NLS/SAL1 REV primers, the EKAR constructs were amplified and cloned into pLenti CMV GFP Hygro (656-4) (Addgene Plasmid #17446). Both the purified PCR inserts and pLenti GFP Hygro were digested with BAMH1 and SAL1, purified, and ligated. Colonies were screened as described above.

Inhibitors

The ERK1/2-selective inhibitor SCH772984 was provided by Merck. The MEK1/2-selective inhibitor, trametinib (GSK1120212), was obtained from Selleckchem, cat. no. S2673. The KRAS^{G12C}-selective inhibitor MRTX1257 was provided by Mirati Therapeutics. The KRAS^{G12D}-selective inhibitor MRTX1133 was provided by Mirati Therapeutics or purchased from Selleckchem, cat. no. E1051. The RAS(ON) multiselective tricomplex inhibitor RMC-7977 was provided by Revolution Medicines.

Antibodies

The following primary antibodies were used for immunoblotting and/or immunofluorescence staining. From Cell Signaling Technology: p44/42 MAPK (ERK1/2) (L34F12), cat. no. 4696 (RRID:AB_390780); phospho-p44/42 MAPK (ERK1/2) (Thr202/Tyr204) (D13.14.4E), cat. no. 4370 (RRID:AB_2315112); MYC-Tag (9B11), cat. no. 2276 (RRID:AB_331783); c-MYC (D84C12), cat. no. 5605 (RRID:AB_1903938); phospho-p90RSK (Thr359/Ser363), cat. no. 9344 (RRID:AB_331650); RSK1/2/3 (32D7), cat. no. 9355 (RRID:AB_659900); phospho-FRA1 (Ser265) (D22B1), cat. no. 5841 (RRID:AB_10835210). From Sigma-Aldrich: Vinculin, cat. no. V9131 (RRID:AB_477629); KRAS (3B10-2F2), cat. no. WH0003845M1 (RRID:AB_1842235). F-actin was stained using phalloidin Alexa Fluor 488, Invitrogen cat. no. A12379, and Alexa Fluor 647, Invitrogen cat. no. A22287. Secondary antibodies used for immunoblotting included IgG (H+L) cross-adsorbed goat anti-mouse, HRP, Invitrogen cat. no. PI31432, and IgG (H+L) cross-adsorbed goat anti-rabbit, HRP, Invitrogen cat. no. PI31462. Secondary antibodies used for immunofluorescence included goat anti-mouse IgG (H+L) Alexa Fluor 568, Invitrogen cat. no. A-11004, goat anti-rabbit IgG (H+L) Alexa Fluor 568, Invitrogen cat. no. A-1101, and goat anti-rabbit IgG (H+L) Alexa Fluor 488, Invitrogen cat. no. A-11008. Antibodies used for RPPA are listed in table S3.

Viral transduction

HEK293T cells (0.9×10^6) were plated in T25 flasks in DMEM supplemented with 10% FBS. After 24 hours the cells were transfected using 500 μ l of Optimem combined with 25 μ l of Fugene 6 (Promega), 3 μ g of psPax, 1 μ g of

pMD2.G, and 4 μ g of target construct. After 24 hours the medium was replaced with DMEM supplemented with 20% FBS. Viral particles were generated over 48 hours at which point supernatant was removed and filtered through a 0.45 μ m PES syringe filter (Nalgene). Filtered supernatant was either aliquotted and frozen at -80°C or used directly to infect target cells. Supernatant was combined with polybrene (8 μ g/ml) and diluted in either DMEM or RPMI with 10% FBS to infect. Culture medium was changed 12 hours post infection and selection was initiated 48 hours after transduction.

siRNA transfections

All siRNA transfections were performed using lipofectamine RNAiMax (ThermoFisher, cat. no. 13778150), and 10 nM of siRNA in Optimem. RNAiMax was added to Optimem and incubated for 5 min at room temperature, then siRNA(s) were then added and incubated 20 min. The siRNAs and cells were combined and incubated for 72 hours for cell lysates or 6 days for growth assays. Non-targeting controls were used in each experiment. The siRNAs utilized are listed in table S4.

Growth assays

Cells were plated in 96-well plates (1000 to 2000 cells per well) and grown for 24 hours. An additional day 0 plate was also prepared. For Dox-inducible cell lines, either Dox or vehicle (dimethyl sulfoxide, DMSO) was added to cells during plating. Pharmacological inhibitors were added to cells after 24 hours using a Tecan D300e digital dispenser; additionally, the day 0 plate was labeled with calcein AM (cells) or Hoechst (nuclei) and counted live. Treated cells were incubated for designated times. Calcein AM or Hoechst was added and were counted using either a SpectraMax i3X multimode detection platform (Molecular Devices) for calcein AM labeled cells and a BioTek Cytation 1 (Agilent) for Hoechst labeled cells. Day 0 plates were used to calculate fold growth to verify cells were growing as expected between biological replicates. Growth percentage was calculated for each biological by normalizing treated values to their control samples, which were set to 100%. Three-parameter drug response curves were generated using the average relative growth (%) from ≥ 3 biological replicates in GraphPad Prism version 9.3.1. Error bars represent the standard error of the mean between biological replicates.

Immunofluorescence staining and imaging

Cells were plated on glass bottom dishes and imaged using an EVOS M7000 wide-field microscope with a 40X, 0.65 NA objective. Cells were fixed with 4% formaldehyde for 20 min, permeabilized with 0.1% Triton for 5 min, rinsed with PBS, and blocked using 3% BSA-PBS for 1 hour, all at room temper-

ature. Primary antibodies targeting: pERK1/2, ERK1/2, and MYC were diluted 1:200 in 3% BSA-PBS and either incubated for 2 hours at room temperature or overnight at 4°C. Cells were washed with PBS and then incubated for 45 min with Alexa-488 and/or Alexa-561 secondary antibodies diluted 1:200 in 1% BSA-PBS at room temperature. Cells were stained for F-actin using phalloidin tagged with either Alexa Fluor 488 or 647. Phalloidin was diluted 1:100 in PBS and cells were stained for 20 min at room temperature. Nuclei were visualized by staining cells for 4',6-diamidino-2-phenylindole (DAPI) diluted 1:10,000 in PBS for 5 to 10 min following secondary antibody staining at room temperature. Cells were washed multiple times using PBS and stored in PBS at 4°C until imaging.

EKAR live cell imaging

Pa16C cells stably expressing EKAR4, nuc-EKAR4, or cyto-EKAR4 were plated on glass bottom dishes and imaged live using an EVOS M7000 wide-field microscope with a 40X, 0.65 NA objective. Upon drugging, cells were washed with PBS and phenol red-free DMEM +10% FBS was added.

Image analysis

For all images, background was removed using a sliding paraboloid in FIJI. The resulting images were analyzed using Cell Profiler. For the immunofluorescence images, the DAPI images were used to identify the primary objects (nuclei) and the total ERK1/2 antibody was used to identify secondary objects (cells). All cells and nuclei touching the edges were discarded. The integrated density for phospho-ERK1/2 was calculated within nuclei and cells, and MYC was calculated within the nuclei, where it was almost entirely localized. To quantify F-actin, primary objects (nuclei) were identified again using the DAPI images and secondary objects (cells) using the F-actin images. The integrated density for F-actin was calculated for each cell. Cell size was calculated by outlining individual cells in FIJI. For EKAR-expressing cells, the primary objects were identified using the yellow fluorescent protein (YFP) channel, cells touching the edge were removed, and the integrated density for each cell was measured in the cyan fluorescent protein (CFP) and fluorescence resonance energy transfer (FRET) channels. The FRET ratio was determined by dividing the FRET value by the CFP value for each cell. For each biological replicate, the mean value of the DMSO sample was calculated and all values were divided by that mean value. From each biological replicate, 5 to 10 frames were collected. Because no statistical difference was observed in the relative integrated density between replicates, all nuclei or cells were grouped together. Table S5 lists the number of cells analyzed for each condition. GraphPad Prism version 9.3.1 was used

for statistical analyses and removal of outliers (using Q=0.1, ROUT) (82). Significance was evaluated using a one-way analysis of variance (ANOVA) and Kruskal-Wallis test relative to DMSO.

Immunoblot analyses

Following the designated treatments, cell lysates were prepared as follows: Cells were washed with cold PBS and then scraped into lysis buffer (50 mM Tris-HCl pH 7.5, 150 mM NaCl, 1% NP-40 (Igepal CA-630), 0.5% sodium deoxycholate, 0.1% SDS) supplemented with protease (Roche) and phosphatase (Sigma-Aldrich) inhibitors. Lysates were incubated 10 min on ice, centrifuged at 8000 rpm (4°C for 10 min), and supernatant was transferred to a new tube. Bio-Rad Protein Assay Dye Reagent cat. No. 5000006 was used to determine protein concentration. Equal amounts of protein were combined with 4X Laemmli SDS sample buffer and 2.5% 2-mercaptoethanol and loaded into SDS-polyacrylamide gel electrophoresis gels. Immunoblots were performed using standard procedures. Immunoblot levels were analyzed using FIJI.

Reverse-phase protein array

Reverse-phase protein array (RPPA) was performed as previously described (31, 42, 57–61). In brief, PDAC cell lines were reverse transfected with a non-targeting (NS) siRNA or siRNAs targeting KRAS (*KRAS*), ERK2 (*MAPK1*), ERK1 (*MAPK3*), or ERK2/ERK1 (*MAPK1/3*). Two siRNAs for each gene were used and four biological replicates for each treatment were performed. A list of siRNAs used is found in table S3. Cells were collected 72 hours post transfection, and cell lysates were prepared as previously described (31, 42, 57–61). Samples were directly lysed from the six-well plates using a buffer containing a 1:1 solution of Tissue Protein Extraction Reagent (Pierce) and 2X Tris-Glycine SDS Sample Buffer (Invitrogen Life Technologies) supplemented with 2.5% of 2 β-mercaptoethanol (Sigma Aldrich). The lysates were heated at 100°C for 8 min and stored at -80°C until RPPA was performed.

Each sample was printed in triplicate on nitrocellulose-coated glass slides (Grace Bio-Labs) using an Aushon 2470 arrayer (Quanterix) outfitted with 185 μm pins. To ensure RPPA assay quality and data reliability, two twelve-point standard curves were prepared as previously described (62) and printed on each slide along with the samples. Before immunostaining, each slide was treated for 15 min at room temperature with Reblot Plus Mild Antibody Stripping Solution (MilliporeSigma) followed by incubation for five hours with I-Block (Invitrogen), a protein-based blocking reagent. Immunolabeling was performed using an automated Autostainer (Agilent Technologies). Arrays were first treated with a 3% hydrogen peroxide, biotin blocking

system, and then a serum free protein block. Arrays were probed with a total of 150 antibodies (table S2) to measure protein expression and activation of markers involved in signaling pathways that control cell growth, survival and metabolism.

Before their use on RPPA, all antibodies were rigorously validated for specificity, selectivity and optimal concentration as previously described (63). Incubation with the primary antibodies was performed for 30 min at room temperature followed by incubation for 15 min in goat anti-rabbit, mouse, or rat (Vector Laboratories) biotinylated secondary antibody. For each staining batch, one slide was incubated with the secondary antibody alone as a negative control for the nonspecific background. The commercially available GenPoint kit (Agilent Technologies) based on tyramide avidin/biotin signal amplification coupled with the fluorescent IRDye 680 Streptavidin (Li-Cor Biosciences) was used for signal detection. The total protein amount for each sample was assessed by staining one in every 15 slides with Sypro Ruby Protein Blot Stain (Invitrogen) following manufacturer's instructions. Slides were treated with a fixative solution (10% v/v methanol and 7% v/v acetic acid) at room temperature for 15 min, washed in deionized water, and stained with Sypro Stain for 30 min at room temperature in the dark. Slides were washed twice in deionized water and dried before scanning. Image acquisition for Sypro Ruby, control and antibody-stained slides was performed using a Tecan scanner (TECAN) using two different wavelength channels at 580 nm (for the Sypro stained slides) and 620 nm (for the antibody stained and control slides). Data analysis was performed using MicroVigene software, version 5.1.1.1 (VigeneTech, Inc). This software includes automatic spot finding, background subtraction, total protein normalization and replicates average as previously described (64). The final RPPA intensity value output for each sample is the average of the replicates printed on the arrays, a single value for every marker analyzed in this study.

Antibody intensities were \log_2 transformed and median centered by the NS control. Differential expression was performed by linear models for microarray and RNAseq data (LIMMA) (65, 66). When considering all cell lines together, individual cell lines were used as a blocking term (67).

RNA-seq analysis

RNA sequencing (RNA-seq) was conducted on Pa16C cells expressing ERK1^{SD}, ERK2^{SD}, or green fluorescent protein (GFP) upon 24 hours of treatment with KRASi (MRTX1133) or control (DMSO). Total RNA was isolated from Pa16C cells constitutively expressing activated ERK1^{SD} (R84S/S170D), ERK2^{SD} (R67S/S153D),

or GFP control treated for 24 hours with 100 nM MRTX1133 or equivalent DMSO. Two biological replicates were prepared for each condition. cDNA libraries were prepared from mRNA isolated by poly(A) mRNA strand purification of total RNA by Novogene (Sacramento, CA) and sequenced on an Illumina NovaSeq2000. RNA-seq data analyses were performed as described (7). Repressed gene expression was determined by comparing expression changes of top differentially expressed genes ($|log_2FC| > 0.25$, FDR < 0.01) in GFP control cells to ERK1^{SD}- or ERK2^{SD}-expressing cells. ERK1 treatment followed by RNA-seq of PDAC cell lines (HPAC, HPAFII, Pa01C, Pa04C, Pa14C, and PANC-1) was described previously (31).

RNA-seq data preprocessing and analyses

TrimGalore (v0.4.5) (68) was used for quality control and to trim adapters of RNA-seq data where necessary, retaining paired end reads of >35 bases in length and >28 quality score (Sanger/Illumina 1.9). The human genome version hg38 (GRCh38.p12) was used for alignment with STAR (v2.7.8a) (69) and the Gencode (v30) (70) basic transcriptome. Transcripts were quantified using Salmon (v0.11.3) (71) and then summarized at the gene level with tximport (v1.22.0) (72). BiomaRt (v2.50.3) (73) was used for annotation and edgeR (v3.36.0) was used for data management (74). Autosomal and X-linked protein coding genes were evaluated with TMM (75) normalization and differential expression comparisons with the glmQLFTest function (edgeR).

Kinome enrichment – MIB-MS

Data for cell lines treated for 24 hours with SCH772984 (1 μM) and subjected to MIB-MS analyses were published previously (76) (PRIDE ID: PXD025819). Data for cell lines treated for 1 hour with SCH772984 (1 μM) were generated as described previously (76). Briefly, lysates from treated cells were prepared in MIB-MS lysis buffer (50 mM HEPES [pH 7.5], 0.5% Triton X-100, 150 mM NaCl, 1 mM EDTA, 1 mM EGTA, 10 mM sodium fluoride, 2.5 mM sodium orthovanadate, protease inhibitor cocktail (Roche), 1% each of phosphatase inhibitor cocktails i and ii (Sigma-Aldrich). Lysates were sonicated 4x with 15-s pulses followed by centrifugation (10 min, 13,200 rpm, 4°C). Supernatants were clarified by 0.2 mm filter and stored at -80°C. Lysates were passed over multiplexed kinase inhibitor beads by gravity (Sepharose conjugated to VI-16832, CTx-0294885, PP58, Purvalanol B, UNC8088A, and UNC21474). Beads were washed first with high salt (1 M NaCl) followed by low-salt (150 mM NaCl + 0.1% SDS) buffers. Kinases were eluted by boiling beads for 5 min in elution buffer (100 mM Tris-HCl [pH 6.8], 0.5% SDS, 1% β-mercaptoethanol). Eluted kinases were reduced (dithiothreitol) and alkylated (iodoacetamide) before concentration

with 10 kD MWCO (Amicon Ultra-4) and subsequent chloroform/methanol extraction. Protein pellets were resuspended (50 mM HEPES, pH 8.0) and digested with sequencing grade trypsin (Promega) overnight at 37°C. Peptides were purified using PepClean C18 Spin Columns (Thermo Scientific).

Kinome LC-MS/MS and data analysis

Purified peptides were analyzed by LC-MS/MS by an Easy nLC 1000 coupled to a Qexactive HF mass spectrometer (Thermo Scientific) operated in data-dependent mode using the top 15 ions. Peptides were separated by an Easy Spray PrepMap C18 column (75 μm × 25 cm × 2 μm particles; Thermo Scientific) in water with 0.1% formic acid subjected to gradient separation of 5–32% Acetonitrile with 0.1% formic acid at 250 nL/min for 2 hours. Precursor resolution (m/z 400 to 1600) was set to 120,000 with a target of 3×10^6 ions and normalized collision energy set at 27% for HCD. Peptides with unknown charge or charge of 1 and ≥ 8 were excluded. Raw data files were analyzed in MaxQuant (77) (MQ) version 1.5.3.17 and searched against Uniprot Human Reference Proteome (78) (20,203 sequences, accessed August 2015) and known contaminants in MQ using Andromeda search engine (79). Spectra were matched between runs (2 min match window, 20 min alignment window). Protease was set to trypsin with up to two missed cleavages with carbamidomethylation of cysteine set as a fixed modification and oxidation of methionine as a variable modification with 1% FDR. Sample analyses were performed in R (4.2.2). LFQ intensities were first filtered for known human kinases annotated in KinHub that had >2 unique razor peptides with a score > 5 . Samples were \log_2 transformed and median normalized. Sample quality was assessed by principal component analysis and pearson correlation. Proteins not detected in at least 60% of the samples were removed, and protein intensities were median centered by the median in control samples (DMSO treated). Differential expression was performed by linear models for microarray and RNAseq data (LIMMA) (65, 66) using the individual cell lines as a blocking term (67) when considering all cell lines together. Missing data was not imputed.

Sample preparation for proteomics analysis

For ERKi, MIA PaCa-2, PANC-1, HPAC, Panc 10.05, ASPC-1 and SW1990 were treated with either 1 μM SCH772984 or equivalent volume DMSO for 1 or 24 hours. For G12Ci, H358, SW837, and MIA PaCa-2 cells were treated with either 20 nM MRTX1257 or equivalent DMSO for 24 or 72 hours. For RASi, K8484 cells were treated with either 10 nM RMC-7977 or equivalent DMSO for 24 hours. Cell lysates were prepared in 400 to 450 μL of lysis buffer [8 M urea, 50 mM NH₄HCO₃ (pH 7.5),

1x protease inhibitor cocktails (Roche) and 1x phosphatase inhibitor cocktails I and II (Sigma-Aldrich)]. Lysates were sonicated six times (15 s at 30% frequency, 90 s on ice). Following sonication, samples were centrifuged for 10 min at 14,000 rpm at 4°C. Supernatants were then passed through a 0.2 μm filter before cryo-storage at -80°C. Cell lysates were submitted to the UNC Proteomics Core for additional preparation.

Cell lysates (1 mg per sample) were reduced with 5 mM DTT (45 min at 37°C) and alkylated with iodoacetamide (15 mM for 30 min in the dark at room temperature). Protein was precipitated at a 1:10 ratio with cold methanol. Precipitates were centrifuged at 5000 rpm at 4°C for 45 min and protein pellets were reconstituted in 50 mM ammonium bicarbonate pH 8 to achieve a 0.5 mg/ml concentration. Samples were digested with LysC (Wako, 1:75 w/w) for 2 hours at 37°C, then digested with trypsin (Promega, 1:75 w/w) overnight at 37°C. The resulting peptide samples were acidified, desalting using desalting spin columns (Thermo), then the eluates were dried via vacuum centrifugation. Peptide concentration was determined using Quantitative Colorimetric Peptide Assay (Pierce).

For ERKi and RASi treated cells, 16 total samples per cell line were labeled with TMTpro 16plex reagents (Thermo Fisher). For G12Ci treated cells, ten samples were labeled with TMTpro 10plex reagents (Thermo Fisher). Each sample (125 μg ERKi/G12Ci, 200 μg RASi) was reconstituted with 50 mM HEPES pH 8.5, then individually labeled with TMTpro reagent (250 μg ERKi/G12Ci, 500 μg RASi) for 1 hour at room temperature. Labeling efficiency was evaluated by LC-MS/MS analysis of a pooled sample consisting of 1 μL of each sample. After confirming >98% efficiency, samples were quenched with 50% hydroxylamine to a final concentration of 0.4%. Labeled peptide samples were combined 1:1, desalting using Thermo desalting spin columns, and dried via vacuum centrifugation. The dried TMT-labeled samples were fractionated using high-pH reversed-phase high-performance liquid chromatography (rpHPLC) (30). Briefly, the samples were offline fractionated into 96 fractions over a 90 min run by high-pH rpHPLC (Agilent 1260) using an Agilent ZORBAX 300Extend-C18 column (3.5-μm, 4.6 × 250 mm) with mobile phase A containing 4.5 mM ammonium formate (pH 10) in 2% (vol/vol) LC-MS grade acetonitrile, and mobile phase B containing 4.5 mM ammonium formate (pH 10) in 90% (vol/vol) LC-MS grade acetonitrile. The 96 resulting fractions were then concatenated in a noncontinuous manner into 24 fractions and 5% of each was aliquotted, dried down through vacuum centrifugation, and stored at -80°C until further analysis.

The remaining 95% of each fraction was further concatenated into four fractions and

dried down via vacuum centrifugation. For each fraction, phosphopeptides were enriched using the High Select Fe-NTA kit (Thermo). For ERKi and G12Ci treated samples, flow-through was enriched a second time using the High Select TiO₂ kit (Thermo). Manufacturer protocols were followed for both enrichments. Fe-NTA and TiO₂ elutes were dried down via vacuum centrifugation and stored at -80°C until further analysis.

LC-MS/MS analysis

The proteome fractions and phosphoproteome fractions (FeNTA and TiO₂ elutes) for ERKi and G12Ci treated samples were analyzed by LC-MS/MS using an Easy nLC 1200 coupled to an Orbitrap Fusion Lumos Tribrid mass spectrometer (Thermo Scientific). The proteome and phosphoproteome fractions (FeNTA elutes) for RASi treated samples were analyzed by LC-MS/MS using a Thermo Ultimate3000 nanoLC coupled to an Exploris480 mass spectrometer (Thermo Scientific). ERKi/G12Ci treated samples were injected onto an Easy Spray PepMap C18 column (75 μm id × 25 cm, 2 μm particle size) (Thermo Scientific) and separated over 120 min. The gradient for separation consisted of 5 to 42% mobile phase B at a 250 nL/minute flow rate, where mobile phase A was 0.1% formic acid in water and mobile phase B consisted of 0.1% formic acid in 80% ACN. RASi treated samples were injected onto an Ion Opticks Aurora C18 column (75 μm id × 15 cm, 1.6 μm particle size) and separated over 70 or 100 min. The gradient for separation consisted of 5–42% mobile phase B at a 250 nL/minute flow rate, where mobile phase A was 0.1% formic acid in water and mobile phase B consisted of 0.1% formic acid in 80% ACN.

For the ERKi proteome fractions, the Lumos was operated in SPS-MS3 mode (80), with a 3 s cycle time. Resolution for the precursor scan (m/z 400 to 1500) was set to 120,000 with an AGC target set to standard and a maximum injection time of 50 ms. MS2 scans consisted of CID normalized collision energy (NCE) 32; AGC target set to standard; maximum injection time of 50 ms; isolation window of 0.7 Da. Following MS2 acquisition, MS3 spectra were collected in SPS mode (10 scans per outcome); HCD set to 55; resolution set to 50,000; scan range set to 100–500; AGC target set to 200% with a 100 ms maximum inject time.

For the phosphoproteome fractions, the Lumos was operated in MS2 mode (28, 29) with a 3-s cycle time. Resolution for the precursor scan (m/z 400–1500) was set to 60,000 with an AGC target set to standard and a maximum injection time of 50 ms. For MS2 scans, HCD was set to 35; AGC target set to 200%; maximum injection time of 120 ms; isolation window of 0.7 Da; resolution set to 50,000. The Exploris480 was operated in turboTMTpro mode

with a cycle time of 3 s. Resolution for the precursor scan (m/z 375 to 1400) was set to 60,000 with an AGC target set to standard and a maximum injection time set to auto. MS2 scans (30,000 resolution) consisted of higher collision dissociate (HCD) set to 38; AGC target set to 300%; maximum injection time set to auto; isolation window of 0.7 Da; fixed first mass of 110 m/z .

Proteomics MS search

All MS raw files were jointly searched by treatment condition (ERKi/G12Ci/RASi) using the MQ (77) 2.4.3.0 Andromeda search engine (79) and the UniProt Human Reference Proteome (78) (20,586 sequences, accessed August 2023) for ERKi/G12Ci-treated samples or UniProt Mouse Reference Proteome (21,864 sequences, accessed October 2023) for RASi treated samples, and known contaminants included in MQ. The peptide length was set to 8–25 with a maximum mass of 4,600 Da. False Discovery Rate (FDR) for peptide identification was set at <0.01 with a minimum of one razor peptide. Peptide search was matched between runs with a match time window of 0.7 min.

For identification of modified peptides, MS2 reporter ion for TMTpro-16plex or 10plex (Thermo) was searched using manufacturer's isotope correction factors with a reporter mass tolerance of 0.003 Da. Reporter ions were filtered by a minimum precursor intensity fraction (PIF) of 0.75. Oxidation, N-terminal acetylation, and phospho-serine-threonine-tyrosine (STY) were set as variable modifications, and carbamidomethyl was set as fixed modifications with a maximum number of five modifications per peptide. Digestion was set to Trypsin/P with three maximum missed cleavages. Default orbitrap settings were used for spectrometer.

To reduce ratio compression for global proteomics (81), unmodified peptides were searched by MS3 reporter ion for TMTpro-16plex (Thermo) using manufacturer's isotope correction factors and mass tolerance of 0.003 Da. Oxidation and N-terminal acetylation were set as variable modifications, and carbamidomethyl was set as fixed modifications. All other settings were the same as for modified peptide search.

Proteomics differential expression analysis

Global proteomic and phosphoproteomic differential expression analysis was performed in R (v4.2.2) using LIMMA (65). Contaminants and reverse sequences were removed, and sample intensities were \log_2 transformed and median normalized. Sample quality was assessed by total intensity distributions, principal component analysis, and sample correlation analyses. For phosphoproteomics samples, phosphosites were filtered for Class I phosphosite assignment (localization probability $> 75\%$). Proteins and phosphosites were median centered by

the median of control samples (DMSO) before performing differential expression analysis (66). When considering all cell lines together, individual cell lines were used as a blocking term (67). Missing data was not imputed.

Database comparisons

The CPTAC PDA dataset was prepared using Supplemental Table S3 from Cao *et al.* (2021) (26) with reported differential expression of phosphosites in tumors versus non-adjacent normal tissues. Differentially regulated phosphosites were defined as having a false-discovery rate of <0.05 . The ERK Compendium dataset was prepared from Unal *et al.* (2017) (21). The databases of known regulatory sites, phosphosites with Cell Signaling Technologies antibodies, and all annotated PSP phosphosites were prepared from PhosphoSitePlus (25) and filtered for human phosphosites. The PTMsigDB dataset was prepared by downloading the human PTMsigDB set (v1.9.0) (82). The functional human phosphoproteome was prepared from Supplementary Table S43 from Ochoa *et al.* (2019) (27). A database of annotated human kinases was prepared from KinHub. Transcription factors were annotated from Supplemental Table S1 from Lambert *et al.* (2018) (83) and filtered for transcription factors. Protein phosphatases were annotated from Supplemental Table S1 from Chen *et al.* (2017) (84) and filtered for proteins within the evolutionarily conserved human protein phosphatome. A catalog of E3 ubiquitin ligases was prepared from UbiNet 2.0 (85). Epigenetic regulators were annotated as published in EpiFactors (86, 87). Proteins involved in epigenetic regulation contain proteins annotated to be kinases, transcription factors, phosphatases, or ubiquitin E3 ligases, and these proteins were filtered out of the epigenetic dataset. Other than the epigenetic regulators, other protein groups were found to be mutually exclusive. The membership of each phosphosite or phosphoprotein within each of these datasets was annotated in phosphoproteomics data and used for further analysis.

Human-mouse phosphosite alignment

Gene names of phosphoproteins were converted from human to mouse homologs using msigdb (v7.5.1). Gene names were matched to the FASTA names in the UniProt Mouse Reference Proteome (21,864 sequences, accessed October 2023). Each 15-amino acid flanking sequence identified on each phosphoprotein was aligned to the full protein amino acid sequence of the corresponding mouse homolog using the ClustalOmega method in the multiple sequence alignment (msa) package (v1.32.0) (88). Pairwise distances of the two aligned sequences were computed using seqinr (v4.2-36) (89) to assign an alignment score.

Subcellular localization and motif analyses

Assignment of subcellular localization of proteins was determined by the max score reported by Binder *et al.* (2014) (90) for main subcellular compartments (nucleus, cytoplasm, mitochondrion, lysosome, plasma membrane, cytoskeleton, endosome, peroxisome, and Golgi apparatus).

D motifs were determined by the greater MEF2A D motifs reported in Supplementary Table 1 of Zeke *et al.* (2015) (91) with the addition of RPS6 kinases RPS6KA1-6 and RPS6KB1-2. DEF motifs were identified by regular expression search within the amino acid sequence of each uniprot ID for the amino acid pattern [F/W]-X-[F/W/Y]-P, where X is any amino acid.

Overrepresentation was determined by one-tailed hypergeometric testing using all detected phosphosites or phosphoproteins at each respective timepoint as the background and P values adjusted by the Benjamini-Hochberg procedure. Enrichment was determined by the relative proportion detected in the foreground to the proportion detected in the background.

Phosphoprotein enrichment and network analyses

Gene sets were downloaded from the Molecular Signatures Database (V7.4) and filtered for Reactome gene sets. Overrepresentation was determined by one-tailed hypergeometric testing and p values adjusted by Benjamini-Hochberg with a minimum background set to five phosphoproteins. Enrichment was determined by the relative proportion of representation in the foreground to the proportion in the background. Networks were generated in R (v4.2.2) using the top ten significantly enriched gene sets. Phosphoproteins with differentially regulated phosphosites ($P < 0.05$) and gene sets were defined as the nodes, and edges were defined as the membership of each phosphoprotein within the gene sets.

Phosphatase enrichment analysis

Phosphatase substrates were determined using data from BioGRID (v4.4.213) by filtering for human interactions from annotated phosphatases that have activity toward protein substrates. Differentially regulated phosphosites were used to determine proteins with down or up-regulated phosphosites ($P < 0.01$). Phosphatase activity enrichment was determined by comparing enrichment of phosphatase substrates with down or up-regulated phosphosites (foreground) to all phosphatase substrates detected (background) using one-tailed hypergeometric testing with p values adjusted by Benjamini-Hochberg. Only phosphatases with a minimum of 20 substrates detected were considered.

Kinase library analysis and network construction

Differentially regulated phosphosites were analyzed for kinase-motif enrichment as reported

previously (37). Relative kinase activities were determined by the product min-max normalized adjusted p values and \log_2 enrichment factor for the most significant enrichment direction for each kinase. Individual phosphosites were scored for the 303 human kinases as described previously (37), and top kinases for phosphosites were filtered for the top 25 scoring kinases by percentile. The first kinase-phosphosite link was assigned a score by taking the product of the kinase-phosphosite percentile and absolute value of the relative kinase activities for each cell line and comparison and defined as the kinase library score. Previously reported kinase-phosphosite evidence was added to the kinase library score by integrating the kinase-substrate dataset available from PhosphoSitePlus (25). A score of 0.5 was added to the kinase library score for each level of evidence, *in vitro* and *in vivo*, reported in the kinase-substrate set. Because the kinase library does not assign a kinase to phosphotyrosine sites, the link for phospho-tyrosines was created by the evidence within the PSP kinase-substrate dataset. The PSP score was added to the kinase library score.

Next, kinase-substrate interactions were annotated from the PhosphoNetworks (38) and BioGRID (39) databases. Kinase-substrate interactions from PhosphoNetworks were assigned a score of 0.5 and added to the kinase library score. Data from BioGRID (v4.4.213) was filtered for human interactions and the score was scaled by the number of references that reported the kinase-substrate interaction [score = $n/(n+1)$, where n is the number of references reporting the interaction]. The BioGRID score for each kinase-substrate interaction was added to the kinase library score.

The final interaction score was determined by taking the product of the final kinase library score and the relative phosphosite differential regulation matched for each cell line and comparison. The relative phosphosite differential regulation was calculated by the product of the min-max normalized adjusted p values and \log_2 fold-change for each cell line and comparison. Each phosphosite was filtered for the top three kinase interaction scores. This score represents the likelihood that a kinase is responsible for regulating that individual phosphosite. The final kinase interaction score for kinase-substrate interactions was defined as the sum of interaction scores for each phosphosite. All computations were performed in R (v4.2.2) and networks were created using the final interaction score for each kinase-substrate as links and each kinase and substrate as nodes. Nodes were annotated by databases as described above.

Kinase tree

Relative kinase activities were plotted in Coral (92) using relative activities described above as node size, branch color, and node color.

Motif analyses

Flanking sequences for the background detected sequences were annotated as position specific frequency matrices (PSFMs). Foreground sequences were determined for indicated kinases by filtering for kinase interactions defined in the kinase-substrate network defined above. Flanking sequences for phosphosites attributed to the indicated kinase within the kinase-substrate network were annotated as PSFMs. Enrichment or depletion was determined by subtracting the foreground PSFM by the background PSFM. Motifs were visualized using the R package ggseqlogo (93) using the determined enrichment/depletion values.

DepMap analyses

Data from DepMap (22Q1) was accessed through ExperimentHub (94). CRISPR Chronos dependency data (EH7523) and cell line mutation calls (EH7526) were retrieved. Mutation calls were used to annotate KRAS mutant status for each cell line, where the amino acid substitutions G12A, G12C, G12D, G12R, G12S, G12V, G13D, Q61H, Q61K, Q61L, or Q61R were considered as KRAS mutant.

Foreground for overrepresentation analyses of ERK regulated phosphoproteins was determined for proteins with median Chronos dependency <-0.5 of the 43 KRAS-mutant PDAC cell lines. Annotated protein localizations and gene set memberships were defined as described above. Overrepresentation was determined by one-tailed hypergeometric testing using the background of all detected phosphoproteins.

KRAS-mutant select genetic dependencies were determined by a two-way ANOVA of Chronos dependency versus KRAS mutation status and cancer type. Cancer types included in these analyses were defined as having at least 10% KRAS-mutant cell lines. The Tukey Honestly Significant Difference (HSD) post hoc test was used to determine statistical significance.

Statistics and reproducibility

The data are represented as described in the figure legends. The number of technical or biological replicates, fields of images used for analysis, statistical cut-offs used to present data, and statistical tests are described in the figure legends and corresponding materials and methods sections. When appropriate, p values were adjusted for multiple hypothesis testing as described in the figure legends and materials and methods.

REFERENCES AND NOTES

- A. Hayashi, J. Hong, C. A. Iacobuzio-Donahue, The pancreatic cancer genome revisited. *Nat. Rev. Gastroenterol. Hepatol.* **18**, 469–481 (2021). doi: [10.1038/s41575-021-00463-z](https://doi.org/10.1038/s41575-021-00463-z); pmid: [34089011](https://pubmed.ncbi.nlm.nih.gov/34089011/)
- M. Drostén, M. Barbacid, Targeting the MAPK Pathway in KRAS-Driven Tumors. *Cancer Cell* **37**, 543–550 (2020). doi: [10.1101/jccell.2020.03.013](https://doi.org/10.1101/jccell.2020.03.013); pmid: [32289276](https://pubmed.ncbi.nlm.nih.gov/32289276/)
- Z. Karouli, E. Gavathiotis, P. I. Poulikakos, New perspectives for targeting RAF kinase in human cancer. *Nat. Rev. Cancer* **17**, 676–691 (2017). doi: [10.1038/nrc.2017.79](https://doi.org/10.1038/nrc.2017.79); pmid: [28984291](https://pubmed.ncbi.nlm.nih.gov/28984291/)
- E. M. Terrell, D. K. Morrison, Ras-Mediated Activation of the Raf Family Kinases. *Cold Spring Harb. Perspect. Med.* **9**, a033746 (2019). doi: [10.1101/cshperspect.a033746](https://doi.org/10.1101/cshperspect.a033746); pmid: [29358316](https://pubmed.ncbi.nlm.nih.gov/29358316/)
- J. E. Klomp, J. A. Klomp, C. J. Der, The ERK mitogen-activated protein kinase signaling network: The final frontier in RAS signal transduction. *Biochem. Soc. Trans.* **49**, 253–267 (2021). doi: [10.1042/BST20200507](https://doi.org/10.1042/BST20200507); pmid: [33544118](https://pubmed.ncbi.nlm.nih.gov/33544118/)
- H. Lavoie, J. Gagnon, M. Therrien, ERK signalling: A master regulator of cell behaviour, life and fate. *Nat. Rev. Mol. Cell Biol.* **21**, 607–632 (2020). doi: [10.1038/s41580-020-0255-7](https://doi.org/10.1038/s41580-020-0255-7); pmid: [32576977](https://pubmed.ncbi.nlm.nih.gov/32576977/)
- J. A. Klomp et al., Defining the KRAS- and ERK-dependent transcriptome in KRAS-mutant cancers. *Science* **384**, eadk0775 (2024). doi: [10.1126/science.adk0775](https://doi.org/10.1126/science.adk0775)
- A. Liberzon et al., The Molecular Signatures Database (MSigDB) hallmark gene set collection. *Cell Syst.* **1**, 417–425 (2015). doi: [10.1016/j.cels.2015.12.004](https://doi.org/10.1016/j.cels.2015.12.004); pmid: [2671021](https://pubmed.ncbi.nlm.nih.gov/2671021/)
- K. Smorodinsky-Atlas et al., Intrinsically active variants of Erk oncogenically transform cells and disclose unexpected autophosphorylation capability that is independent of TEY phosphorylation. *Mol. Biol. Cell* **27**, 1026–1039 (2016). doi: [10.1091/mbc.E15-07-0521](https://doi.org/10.1091/mbc.E15-07-0521); pmid: [26658610](https://pubmed.ncbi.nlm.nih.gov/26658610/)
- M. A. Emrich, A. N. Hoofnagle, A. S. Miller, L. F. T. Eyck, N. G. Ahn, Constitutive activation of extracellular signal-regulated kinase 2 by synergistic point mutations. *J. Biol. Chem.* **276**, 46469–46479 (2001). doi: [10.1074/jbc.M107708200](https://doi.org/10.1074/jbc.M107708200); pmid: [11591711](https://pubmed.ncbi.nlm.nih.gov/11591711/)
- K. Smorodinsky-Atlas, N. Soudah, D. Engelberg, Mutations That Confer Drug-Resistance, Oncogenicity and Intrinsic Activity on the ERK MAP Kinases-Current State of the Art. *Mutations That Confer Drug-Resistance, Oncogenicity and Intrinsic Activity on the ERK MAP Kinases-Current State of the Art. Cells* **9**, 129 (2020). doi: [10.3390/cells9010129](https://doi.org/10.3390/cells9010129); pmid: [31935908](https://pubmed.ncbi.nlm.nih.gov/31935908/)
- X.-X. Sun, Y. Li, R. C. Sears, M.-S. Dai, Targeting the MYC Ubiquitination-Proteasome Degradation Pathway for Cancer Therapy. *Front. Oncol.* **11**, 679445 (2021). doi: [10.3389/fonc.2021.679445](https://doi.org/10.3389/fonc.2021.679445); pmid: [34178666](https://pubmed.ncbi.nlm.nih.gov/34178666/)
- J. B. Fell et al., Identification of the Clinical Development Candidate MRTX849, a Covalent KRAS^{G12C} Inhibitor for the Treatment of Cancer. *J. Med. Chem.* **63**, 6679–6693 (2020). doi: [10.1021/acs.jmedchem.9b02052](https://doi.org/10.1021/acs.jmedchem.9b02052); pmid: [32250617](https://pubmed.ncbi.nlm.nih.gov/32250617/)
- X. Wang et al., Identification of MRTX1133, a Noncovalent, Potent and Selective KRAS^{G12D} Inhibitor. *J. Med. Chem.* **65**, 3123–3133 (2022). doi: [10.1021/acs.jmedchem.1c01688](https://doi.org/10.1021/acs.jmedchem.1c01688); pmid: [34889605](https://pubmed.ncbi.nlm.nih.gov/34889605/)
- A. M. Waters, C. J. Der, KRAS: The Critical Driver and Therapeutic Target for Pancreatic Cancer. *Cold Spring Harb. Perspect. Med.* **8**, a031435 (2018). doi: [10.1101/cshperspect.a031435](https://doi.org/10.1101/cshperspect.a031435); pmid: [29229669](https://pubmed.ncbi.nlm.nih.gov/29229669/)
- E. A. Collisson et al., A central role for RAF→MEK→ERK signaling in the genesis of pancreatic ductal adenocarcinoma. *Cancer Discov.* **2**, 685–693 (2012). doi: [10.1158/2159-8290.CD-11-0347](https://doi.org/10.1158/2159-8290.CD-11-0347); pmid: [22628411](https://pubmed.ncbi.nlm.nih.gov/22628411/)
- M. J. Smith, M. Ikura, Integrated RAS signaling defined by parallel NMR detection of effectors and regulators. *Nat. Chem. Biol.* **10**, 223–230 (2014). doi: [10.1038/nchembio.1435](https://doi.org/10.1038/nchembio.1435); pmid: [24441586](https://pubmed.ncbi.nlm.nih.gov/24441586/)
- C. Kiel, M. Foglierini, N. Kuemmerer, P. Beltrao, L. Serrano, A genome-wide Ras-effector interaction network. *J. Mol. Biol.* **370**, 1020–1032 (2007). doi: [10.1016/j.jmb.2007.05.015](https://doi.org/10.1016/j.jmb.2007.05.015); pmid: [17544445](https://pubmed.ncbi.nlm.nih.gov/17544445/)
- S. Catozzi, M. Halasz, C. Kiel, Predicted ‘wiring landscape’ of Ras-effector interactions in 29 human tissues. *NPJ Syst. Biol. Appl.* **7**, 10 (2021). doi: [10.1038/s41540-021-00170-0](https://doi.org/10.1038/s41540-021-00170-0); pmid: [33580066](https://pubmed.ncbi.nlm.nih.gov/33580066/)
- M. K. Saba-El-Leil, C. Frémien, S. Meloche, Redundancy in the World of MAP Kinases: All for One. *Front. Cell Dev. Biol.* **4**, 67 (2016). doi: [10.3389/fcell.2016.00067](https://doi.org/10.3389/fcell.2016.00067); pmid: [27446918](https://pubmed.ncbi.nlm.nih.gov/27446918/)
- E. B. Ünal, F. Uhlitz, N. Blüthgen, A compendium of ERK targets. *FEBS Lett.* **591**, 2607–2615 (2017). doi: [10.1002/1873-3468.12740](https://doi.org/10.1002/1873-3468.12740); pmid: [28675784](https://pubmed.ncbi.nlm.nih.gov/28675784/)
- S. Yoon, R. Seger, The extracellular signal-regulated kinase: Multiple substrates regulate diverse cellular functions. *Growth Factors* **24**, 21–44 (2006). doi: [10.1080/02699050500284218](https://doi.org/10.1080/02699050500284218); pmid: [16393692](https://pubmed.ncbi.nlm.nih.gov/16393692/)
- J. S. Duncan et al., Dynamic reprogramming of the kinaseome in response to targeted MEK inhibition in triple-negative breast cancer. *Cell* **149**, 307–321 (2012). doi: [10.1016/j.cell.2012.02.053](https://doi.org/10.1016/j.cell.2012.02.053); pmid: [22500798](https://pubmed.ncbi.nlm.nih.gov/22500798/)

24. S. Klaeger *et al.*, The target landscape of clinical kinase drugs. *Science* **358**, eaan4368 (2017). doi: [10.1126/science.aan4368](https://doi.org/10.1126/science.aan4368); pmid: [29191878](https://pubmed.ncbi.nlm.nih.gov/29191878/)
25. P. V. Hornbeck *et al.*, PhosphoSitePlus. 2014: Mutations, PTMs and recalibrations. *Nucleic Acids Res.* **43**, D512–D520 (2015). doi: [10.1093/nar/gku1267](https://doi.org/10.1093/nar/gku1267); pmid: [25514926](https://pubmed.ncbi.nlm.nih.gov/25514926/)
26. L. Cao *et al.*, Proteogenomic characterization of pancreatic ductal adenocarcinoma. *Cell* **184**, 5031–5052.e26 (2021). doi: [10.1016/j.cell.2021.08.023](https://doi.org/10.1016/j.cell.2021.08.023); pmid: [34534465](https://pubmed.ncbi.nlm.nih.gov/34534465/)
27. D. Ochoa *et al.*, The functional landscape of the human phosphoproteome. *Nat. Biotechnol.* **38**, 365–373 (2020). doi: [10.1038/s41587-019-0344-3](https://doi.org/10.1038/s41587-019-0344-3); pmid: [31819260](https://pubmed.ncbi.nlm.nih.gov/31819260/)
28. A. Hogrefe *et al.*, Benchmarking common quantification strategies for large-scale phosphoproteomics. *Nat. Commun.* **9**, 1045 (2018). doi: [10.1038/s41467-018-03309-6](https://doi.org/10.1038/s41467-018-03309-6); pmid: [29535314](https://pubmed.ncbi.nlm.nih.gov/29535314/)
29. K. Klann *et al.*, Growth Factor Receptor Signaling Inhibition Prevents SARS-CoV-2 Replication. *Mol. Cell* **80**, 164–174.e4 (2020). doi: [10.1016/j.molcel.2020.08.006](https://doi.org/10.1016/j.molcel.2020.08.006); pmid: [32877642](https://pubmed.ncbi.nlm.nih.gov/32877642/)
30. P. Mertins *et al.*, Reproducible workflow for multiplexed deep-scale proteome and phosphoproteome analysis of tumor tissues by liquid chromatography-mass spectrometry. *Nat. Protoc.* **13**, 1632–1661 (2018). doi: [10.1038/s41596-018-0006-9](https://doi.org/10.1038/s41596-018-0006-9); pmid: [29988108](https://pubmed.ncbi.nlm.nih.gov/29988108/)
31. K. L. Bryant *et al.*, Combination of ERK and autophagy inhibition as a treatment approach for pancreatic cancer. *Nat. Med.* **25**, 628–640 (2019). doi: [10.1038/s41591-019-0368-8](https://doi.org/10.1038/s41591-019-0368-8); pmid: [30833752](https://pubmed.ncbi.nlm.nih.gov/30833752/)
32. M. Holderfield *et al.*, Concurrent inhibition of oncogenic and wild-type RAS-GTP for cancer therapy. *Nature* (2024). doi: [10.1038/s41586-024-07205-6](https://doi.org/10.1038/s41586-024-07205-6); pmid: [38589574](https://pubmed.ncbi.nlm.nih.gov/38589574/)
33. F. A. Gonzalez, D. L. Raden, R. J. Davis, Identification of substrate recognition determinants for human ERK1 and ERK2 protein kinases. *J. Biol. Chem.* **266**, 22159–22163 (1991). doi: [10.1016/S0021-9258\(18\)54548-8](https://doi.org/10.1016/S0021-9258(18)54548-8); pmid: [1939237](https://pubmed.ncbi.nlm.nih.gov/1939237/)
34. A. S. Futran, A. J. Link, R. Seger, S. Y. Shvartsman, ERK as a model for systems biology of enzyme kinetics in cells. *Curr. Biol.* **23**, R972–R979 (2013). doi: [10.1016/j.cub.2013.09.033](https://doi.org/10.1016/j.cub.2013.09.033); pmid: [24200329](https://pubmed.ncbi.nlm.nih.gov/24200329/)
35. J. Keyes *et al.*, Signaling diversity enabled by Rap1-regulated plasma membrane ERK with distinct temporal dynamics. *eLife* **9**, e57410 (2020). doi: [10.7554/eLife.57410](https://doi.org/10.7554/eLife.57410); pmid: [32452765](https://pubmed.ncbi.nlm.nih.gov/32452765/)
36. C. A. Dimitri, W. Dowdle, J. P. MacKeigan, J. Blenis, L. O. Murphy, Spatially separate docking sites on ERK2 regulate distinct signaling events in vivo. *Curr. Biol.* **15**, 1319–1324 (2005). doi: [10.1016/j.cub.2005.06.037](https://doi.org/10.1016/j.cub.2005.06.037); pmid: [16051177](https://pubmed.ncbi.nlm.nih.gov/16051177/)
37. J. L. Johnson *et al.*, An atlas of substrate specificities for the human serine/threonine kinase. *Nature* **613**, 759–766 (2023). doi: [10.1038/s41586-022-05575-3](https://doi.org/10.1038/s41586-022-05575-3); pmid: [36631611](https://pubmed.ncbi.nlm.nih.gov/36631611/)
38. J. Hu *et al.*, PhosphoNetworks: A database for human phosphorylation networks. *Bioinformatics* **30**, 141–142 (2014). doi: [10.1093/bioinformatics/btt627](https://doi.org/10.1093/bioinformatics/btt627); pmid: [24227675](https://pubmed.ncbi.nlm.nih.gov/24227675/)
39. R. Oughtred *et al.*, The BioGRID database: A comprehensive biomedical resource for curated protein, genetic, and chemical interactions. *Protein Sci.* **30**, 187–200 (2021). doi: [10.1002/pro.3978](https://doi.org/10.1002/pro.3978); pmid: [33070389](https://pubmed.ncbi.nlm.nih.gov/33070389/)
40. R. Anjum, J. Blenis, The RSK family of kinases: Emerging roles in cellular signalling. *Nat. Rev. Mol. Cell Biol.* **9**, 747–758 (2008). doi: [10.1038/nrm2509](https://doi.org/10.1038/nrm2509); pmid: [18813292](https://pubmed.ncbi.nlm.nih.gov/18813292/)
41. D. J. Wood, J. A. Endicott, Structural insights into the functional diversity of the CDK-cyclin family. *Open Biol.* **8**, 180112 (2018). doi: [10.1098/rsob.180112](https://doi.org/10.1098/rsob.180112); pmid: [30185601](https://pubmed.ncbi.nlm.nih.gov/30185601/)
42. J. E. Klomp *et al.*, CHK1 protects oncogenic KRAS-expressing cells from DNA damage and is a target for pancreatic cancer treatment. *Cell Rep.* **37**, 110060 (2021). doi: [10.1016/j.celrep.2021.110060](https://doi.org/10.1016/j.celrep.2021.110060); pmid: [34852220](https://pubmed.ncbi.nlm.nih.gov/34852220/)
43. A. M. Waters *et al.*, Targeting p130Cas- and microtubule-dependent MYC regulation sensitizes pancreatic cancer to ERK MAPK inhibition. *Cell Rep.* **35**, 109291 (2021). doi: [10.1016/j.celrep.2021.109291](https://doi.org/10.1016/j.celrep.2021.109291); pmid: [34192548](https://pubmed.ncbi.nlm.nih.gov/34192548/)
44. R. G. Hodge, A. J. Ridley, Regulating Rho GTPases and their regulators. *Nat. Rev. Mol. Cell Biol.* **17**, 496–510 (2016). doi: [10.1038/nrm.2016.67](https://doi.org/10.1038/nrm.2016.67); pmid: [27301673](https://pubmed.ncbi.nlm.nih.gov/27301673/)
45. A. Kapoor *et al.*, Yap1 activation enables bypass of oncogenic Kras addiction in pancreatic cancer. *Cell* **158**, 185–197 (2014). doi: [10.1016/j.cell.2014.06.003](https://doi.org/10.1016/j.cell.2014.06.003); pmid: [24954535](https://pubmed.ncbi.nlm.nih.gov/24954535/)
46. D. D. Shao *et al.*, KRAS and YAP1 converge to regulate EMT and tumor survival. *Cell* **158**, 171–184 (2014). doi: [10.1016/j.cell.2014.06.004](https://doi.org/10.1016/j.cell.2014.06.004); pmid: [24954536](https://pubmed.ncbi.nlm.nih.gov/24954536/)
47. S. Mukhopadhyay *et al.*, Genome-Wide CRISPR Screens Identify Multiple Synthetic Lethal Targets That Enhance KRASG12C Inhibitor Efficacy. *Cancer Res.* **83**, 4095–4111 (2023). doi: [10.1158/0008-5472.CAN-23-2729](https://doi.org/10.1158/0008-5472.CAN-23-2729); pmid: [37729426](https://pubmed.ncbi.nlm.nih.gov/37729426/)
48. A. C. Edwards *et al.*, TEAD Inhibition Overcomes YAP1/TAZ-Driven Primary and Acquired Resistance to KRASG12C Inhibitors. *Cancer Res.* **83**, 4112–4129 (2023). doi: [10.1158/0008-5472.CAN-23-2994](https://doi.org/10.1158/0008-5472.CAN-23-2994); pmid: [37934103](https://pubmed.ncbi.nlm.nih.gov/37934103/)
49. A. V. Vaseva *et al.*, KRAS Suppression-Induced Degradation of MYC Is Antagonized by a MEK5-ERK5 Compensatory Mechanism. *Cancer Cell* **34**, 807–822.e7 (2018). doi: [10.1016/j.ccr.2018.10.001](https://doi.org/10.1016/j.ccr.2018.10.001); pmid: [30423298](https://pubmed.ncbi.nlm.nih.gov/30423298/)
50. G. Bollag *et al.*, Clinical efficacy of a RAF inhibitor needs broad target blockade in BRAF-mutant melanoma. *Nature* **467**, 596–599 (2010). doi: [10.1038/nature09454](https://doi.org/10.1038/nature09454); pmid: [20823850](https://pubmed.ncbi.nlm.nih.gov/20823850/)
51. A. Herrero *et al.*, Small Molecule Inhibition of ERK Dimerization Prevents Tumorigenesis by RAS-ERK Pathway Oncogenes. *Cancer Cell* **28**, 170–182 (2015). doi: [10.1016/j.ccr.2015.07.001](https://doi.org/10.1016/j.ccr.2015.07.001); pmid: [26267534](https://pubmed.ncbi.nlm.nih.gov/26267534/)
52. A. Plotnikov *et al.*, the nuclear translocation of ERK1/2 as an anticancer target. *Nat. Commun.* **6**, 6685 (2015). doi: [10.1038/ncomms7685](https://doi.org/10.1038/ncomms7685); pmid: [25819065](https://pubmed.ncbi.nlm.nih.gov/25819065/)
53. A. Vallejo *et al.*, An integrative approach unveils FOSL1 as an oncogene vulnerability in KRAS-driven lung and pancreatic cancer. *Nat. Commun.* **8**, 14294 (2017). doi: [10.1038/ncomms14294](https://doi.org/10.1038/ncomms14294); pmid: [28220783](https://pubmed.ncbi.nlm.nih.gov/28220783/)
54. A. J. Aguirre *et al.*, Activated Kras and Ink4a/Arf deficiency cooperate to produce metastatic pancreatic ductal adenocarcinoma. *Genes Dev.* **17**, 3112–3126 (2003). doi: [10.1101/gad.1158703](https://doi.org/10.1101/gad.1158703); pmid: [14681207](https://pubmed.ncbi.nlm.nih.gov/14681207/)
55. J. Carver *et al.*, A high-throughput assay for small molecule destabilizers of the KRAS oncoprotein. *PLoS ONE* **9**, e103836 (2014). doi: [10.1371/journal.pone.0103836](https://doi.org/10.1371/journal.pone.0103836); pmid: [25093678](https://pubmed.ncbi.nlm.nih.gov/25093678/)
56. J. Keyes, S. Mehta, J. Zhang, Strategies for Multiplexed Biosensor Imaging to Study Intracellular Signaling Networks. Strategies for Multiplexed Biosensor Imaging to Study Intracellular Signaling Networks. *Methods Mol. Biol.* **2350**, 1–20 (2021). doi: [10.1007/978-1-0716-1593-5_1](https://doi.org/10.1007/978-1-0716-1593-5_1); pmid: [34331275](https://pubmed.ncbi.nlm.nih.gov/34331275/)
57. G. A. Hobbs *et al.*, Atypical KRAS^{G12R} Mutant Is Impaired in PI3K Signaling and Macropinocytosis in Pancreatic Cancer. *Cancer Discov.* **10**, 104–123 (2020). doi: [10.1158/2159-8290.CD-19-1006](https://doi.org/10.1158/2159-8290.CD-19-1006); pmid: [31649109](https://pubmed.ncbi.nlm.nih.gov/31649109/)
58. C. M. Goodwin *et al.*, Combination Therapies with CDK4/6 Inhibitors to Treat KRAS-mutant Pancreatic Cancer. *Cancer Res.* **83**, 141–157 (2023). pmid: [36346366](https://pubmed.ncbi.nlm.nih.gov/36346366/)
59. C. A. Stalnecker *et al.*, Concurrent Inhibition of IGF1R and ERK Increases Pancreatic Cancer Sensitivity to Autophagy Inhibitors. *Cancer Res.* **82**, 586–598 (2022). doi: [10.1158/0008-5472.CAN-21-1443](https://doi.org/10.1158/0008-5472.CAN-21-1443); pmid: [34921013](https://pubmed.ncbi.nlm.nih.gov/34921013/)
60. M. V. Huynh *et al.*, Functional and biological heterogeneity of KRAS^{G1} mutations. *Sci. Signal.* **15**, eabn2694 (2022). doi: [10.1126/scisignal.abn2694](https://doi.org/10.1126/scisignal.abn2694); pmid: [35944066](https://pubmed.ncbi.nlm.nih.gov/35944066/)
61. I. Ozkan-Dagliyan *et al.*, Low-Dose Vertical Inhibition of the RAF-MEK-ERK Cascade Causes Apoptotic Death of KRAS Mutant Cancers. *Cell Rep.* **31**, 107764 (2020). doi: [10.1016/j.celrep.2020.107764](https://doi.org/10.1016/j.celrep.2020.107764); pmid: [32553168](https://pubmed.ncbi.nlm.nih.gov/32553168/)
62. M. Pierobon *et al.*, Enrichment of PI3K-AKT-mTOR Pathway Activation in Hepatic Metastases from Breast Cancer. *Clin. Cancer Res.* **23**, 4919–4928 (2017). doi: [10.1158/1078-0432.CCR-16-2566](https://doi.org/10.1158/1078-0432.CCR-16-2566); pmid: [28446508](https://pubmed.ncbi.nlm.nih.gov/28446508/)
63. M. Signore, V. Manganelli, A. Hodge, Antibody Validation by Western Blotting. *Methods Mol. Biol.* **1606**, 51–70 (2017). doi: [10.1007/978-1-4939-6990-6_4](https://doi.org/10.1007/978-1-4939-6990-6_4); pmid: [28501993](https://pubmed.ncbi.nlm.nih.gov/28501993/)
64. E. Pin, G. Federici, E. F. Petricoin, Preparation and use of reverse protein microarrays. *Curr. Protoc. Protein Sci.* **75**, 27.7.1–27.7.29 (2014). doi: [10.1002/0471140864.ps2707s75](https://doi.org/10.1002/0471140864.ps2707s75)
65. M. E. Ritchie *et al.*, limma powers differential expression analyses for RNA-sequencing and microarray studies. *Nucleic Acids Res.* **43**, e47 (2015). doi: [10.1093/nar/gkv007](https://doi.org/10.1093/nar/gkv007); pmid: [25605792](https://pubmed.ncbi.nlm.nih.gov/25605792/)
66. B. Phipson, S. Lee, I. J. Majewski, W. S. Alexander, G. K. Smyth, Robust hyperparameter estimation protects against hypervariable genes and improves power to detect differential expression. *Ann. Appl. Stat.* **10**, 946–963 (2016). doi: [10.1214/16-AOAS920](https://doi.org/10.1214/16-AOAS920); pmid: [28367255](https://pubmed.ncbi.nlm.nih.gov/28367255/)
67. G. K. Smyth, J. Michaud, H. S. Scott, Use of within-array replicate spots for assessing differential expression in microarray experiments. *Bioinformatics* **21**, 2067–2075 (2005). doi: [10.1093/bioinformatics/bti270](https://doi.org/10.1093/bioinformatics/bti270); pmid: [15657102](https://pubmed.ncbi.nlm.nih.gov/15657102/)
68. F. Krueger, Trim Galore! version 0.4.1, Babraham Bioinformatics (2012); http://www.bioinformatics.babraham.ac.uk/projects/trim_galore/.

91. A. Zeke et al., Systematic discovery of linear binding motifs targeting an ancient protein interaction surface on MAP kinases. *Mol. Syst. Biol.* **11**, 837 (2015). doi: [10.1525/msb.20156269](https://doi.org/10.1525/msb.20156269); pmid: [26538579](#)
92. K. S. Metz et al., Coral: Clear and Customizable Visualization of Human Kinome Data. *Cell Syst.* **7**, 347–350.e1 (2018). doi: [10.1016/j.cels.2018.07.001](https://doi.org/10.1016/j.cels.2018.07.001); pmid: [30172842](#)
93. O. Wagih, ggseqlogo: A versatile R package for drawing sequence logos. *Bioinformatics* **33**, 3645–3647 (2017). doi: [10.1093/bioinformatics/btx469](https://doi.org/10.1093/bioinformatics/btx469); pmid: [29036507](#)
94. M. M. Shepherd, ExperimentHub: Client to access ExperimentHub resources. (2024); <https://doi.org/10.18129/B9.bioc.ExperimentHub>.

ACKNOWLEDGMENTS

We thank J. Zhang (UCSD) for EKAR4 plasmids, Revolution Medicines for providing the RAS(ON) multiselective tricomplex inhibitor (RMC-7797), and A. Maitra (MD Anderson Cancer Center) and K. P. Olive (Columbia University) for providing cell lines.

Funding: National Cancer Institute grants R01CA42978, P50CA196510, P50CA257911, U01CA199235, P01CA203657, and R35CA232113 (A.D.C. and/or C.J.D.); Pancreatic Cancer Action Network grant 22-WG-DERB (C.J.D.); Department of Defense grant W81XWH2110692 (C.J.D.); Lustgarten Foundation grant 388222 (C.J.D.); National Cancer Institute grant R35CA197588 (L.C.C.); Pancreatic Cancer Action Network/AACR grant 15-70-25-BRYA (K.L.B.); National Cancer Institute grants P50CA196510 and R37CA251877 (K.L.B.); Department of Defense grant W81XWH2110693 (K.L.B.); Sky Foundation grant (K.L.B.); National Institute of General Medical Sciences grant R01GM138520 (L.M.G.); National Cancer Institute grants T32CA009156, F32CA23932, and K99CA276700 (J.E.K.); American Cancer Society grant PF-20-069 (J.E.K.); SloMo and Cindy Silvian Foundation (J.N.D.); National Cancer Institute grants T32CA071341 and F30CA243253 (J.N.D.); National Institute of General Medical Sciences grant T32GM119999 (A.C.E.); National Cancer Institute grant F31CA275260 (A.C.E.); National Cancer Institute grant T32CA009156 (K.D.M.); American

Cancer Society grant PF-22-066-01-TBE (K.D.M.); National Cancer Institute grants T32CA009156 and F32CA232529 (C.A.S.). This research is based in part upon work conducted using the UNC Proteomics Core Facility, which is supported in part by P30 CA016086 Cancer Center Core Support Grant to the UNC Lineberger Comprehensive Cancer Center. **Author contributions:** Conceptualization: C.J.D., J.N.D., and C.A.S. Experimental design and data analysis: J.N.D., J.E.K., C.J.D., and C.A.S.; Experimental performance: J.E.K., J.N.D., A.C.E., R.Y., A.J.M., K.E.T., K.D.M., K.L.B., A.S., M.P., E.B., A.W.P., N.K.B., L.E.H., and C.A.S.; Data contribution and/or discussions: J.E.K., J.N.D., J.A.K., J.L.J., E.M.H., T.M.Y., L.E.H., E.F.P., L.M.G., L.C.C., and A.D.C.; Computational analysis: led by C.A.S., assisted by J.A.K., E.M.H., and T.M.Y.; Writing: J.E.K., J.A.K., A.D.C., C.J.D., and C.A.S.; All authors reviewed and approved the manuscript. **Competing interests:** C.J.D. was a consultant or advisory board member for Cullgen, Deciphera Pharmaceuticals, Kestrel Therapeutics, Mirati Therapeutics, Reactive Biosciences, Revere Pharmaceuticals, Revolution Medicines Ribometrics, Sanofi, and SHY Therapeutics. C.J.D. has received research funding support from Deciphera Pharmaceuticals, Mirati Therapeutics, Reactive Biosciences, Revolution Medicines, and SpringWorks Therapeutics. A.D.C. has consulted for Eli Lilly and Mirati Therapeutics. M.P. and E.F.P. receive royalties from and are consultants of TheraLink Technologies, Inc. K.L.B. has received research funding support from SpringWorks Therapeutics. E.F.P. is a shareholder and consultant of Avant Diagnostics, TheraLink Technologies, Inc., and Perthera. E.F.P. received funding support from Mirati Therapeutics, Genentech, Inc., and Abbvie, Inc. C.A.S. has received consulting fees from Reactive Biosciences. L.C.C. is a founder and member of the board of directors of Agios Pharmaceuticals and is a founder and receives research support from Petra Pharmaceuticals. L.C.C. is listed as an inventor on a patent (W02019232403A1, Weill Cornell Medicine) for combination therapy for PI3K-associated disease or disorder and the identification of therapeutic interventions to improve response to PI3K inhibitors for cancer treatment. L.C.C. is a cofounder and shareholder in Faeth Therapeutics and has equity in and consults for Cell Signaling

Technologies, Volastra, Larkspur, and 1 Base Pharmaceuticals and consults for Loxo-Lilly. T.M.Y. is a cofounder and stockholder and is on the board of directors of DESTROKE. J.L.J. has received consulting fees from Scorpion Therapeutics and Volastra Therapeutics. The other authors declare no competing interests.

Data and materials availability: All data supporting the findings in this study are provided in the paper or supplementary materials or are deposited in public repositories as described below. Methods of analysis needed to reproduce these observations are described in the materials and methods. Requests for materials related to this study should be addressed to C.A.S. Plasmids can be found on Addgene using the ID numbers listed in the materials and methods. MIB-MS, phosphoproteomic, and global proteomic data have been deposited to the ProteomeXchange Consortium via the PRIDE partner repository. ERKi MIB-MS data are available with identifier PXD043585, and phosphoproteomic and global proteomic data are available with the identifiers PXD048529 (10.6019/PXD048529) and PXD048531 (10.6019/PXD048531). G12C1 and RASi phosphoproteomic data are available with identifiers PXD048532 (10.6019/PXD048532) and PXD048534 (10.6019/PXD048534). The RNA-seq data used in this study have been deposited to the NCBI Sequence Read Archives (SRA) (ERK1/2^{SD} with KRASi, PRJNA1056120) or have been published previously ([31](#)) (ERK1 time series, NCBI SRA PRJEB25806). **License information:** Copyright © 2024 the authors, some rights reserved; exclusive licensee American Association for the Advancement of Science. No claim to original US government works. <https://www.science.org/about/science-licenses-journal-article-reuse>

SUPPLEMENTARY MATERIALS

science.org/doi/10.1126/science.adk0850

Figs. S1 to S6

Tables S1 to S5

Data S1 to S8

MDAR Reproducibility Checklist

Submitted 1 August 2023; accepted 17 April 2024
10.1126/science.adk0850